A CHANDRA STUDY OF SUPERNOVA REMNANTS IN THE LARGE AND SMALL MAGELLANIC CLOUDS

by

ANDREW COREY SCHENCK

Presented to the Faculty of the Graduate School of
The University of Texas at Arlington in Partial Fulfillment
of the Requirements
for the Degree of

DOCTOR OF PHILOSOPHY

THE UNIVERSITY OF TEXAS AT ARLINGTON
May 2017

To my wife, without whom I would never have achieved my dream.

And to my son Fisher Nathaniel Schenck. I miss you terribly.

ACKNOWLEDGEMENTS

The journey up to this point has been a long one. It has had its ups and downs, its share of fun and anxiety, but time has now come to close this chapter in my life and begin the next.

I must start by thanking Sangwook Park, for your patience, advice, and guidance throughout my graduate career. I feel honored to have worked along side you and deeply appreciate everything you have done for me.

Thanks are also due to the other members of this thesis committee, Manfred Cuntz, Yue Deng, Alex Weiss, and Zizislaw Musielak. Thank you for your time and support during my stay at UTA. With a special thanks to Chris Jackson, I appreciate everything.

To our collaborators, David Burrows, Jack Hughes, Jae-Joon Lee, and Koji Mori, thanks for contributing your time and expertise.

Finally, thanks to my colleagues and many friends at UTA, Jayant Bhalerao, Seth Post, and Carola Ellinger to name only a few. Thanks for putting up with me throughout these years and I appreciate you being a part of this journey.

April 14, 2017

ABSTRACT

A CHANDRA STUDY OF SUPERNOVA REMNANTS IN THE LARGE AND SMALL MAGELLANIC CLOUDS

Andrew Corey Schenck, Ph.D.

The University of Texas at Arlington, 2017

Supervising Professor: Dr. Sangwook Park

In the first part of this thesis we measure the interstellar abundances for the elements O, Ne, Mg, Si, and Fe in the Large Magellanic Cloud (LMC), based on the observational data of sixteen supernova remnants (SNRs) in the LMC as available in the public archive of the *Chandra* X-ray Observatory (*Chandra*). We find lower abundances than previous measurements based on a similar method using data obtained with the *Advanced Satellite for Astrophysics and Cosmology* (*ASCA*). We discuss the origins of the discrepancy between our *Chandra* and the previous *ASCA* measurements. We conclude that our measurements are generally more reliable than the *ASCA* results thanks to the high-resolution imaging spectroscopy with our *Chandra* data, although there remain some systematic uncertainties due to the use of different spectral modelings between the previous work and ours. We also discuss our results in comparison with the LMC abundance measurements based on optical observations of stars.

The second part of this thesis is a detailed study of a core-collapse SNR B0049–73.6 in the Small Magellanic Cloud (SMC). Based on our deep *Chandra* observation,

we detect metal-rich ejecta features extending out to the outermost boundary of B0049-73.6, which were not seen in the previous data. We find that the central nebula is dominated by emission from reverse-shocked ejecta material enriched in O, Ne, Mg, and Si. O-rich ejecta distribution is relatively smooth throughout the central nebula. In contrast the Si-rich material is highly structured. These results suggest that B0049-73.6 was produced by an asymmetric core-collapse explosion of a massive star. The estimated abundance ratios among these ejecta elements are in plausible agreement with the nucleosynthesis products from the explosion of a 13-15$M_{\odot}$ progenitor. We reveal that the central ring-like (in projection) ejecta nebula extends to $\sim$9 pc from the SNR center. This suggests that the contact discontinuity (CD) may be located at a further distance from the SNR center than the previous estimate ($\sim$6 pc). Based on our estimated larger size of the CD, we suggest that the significant effect from the presence of a Fe-Ni bubble at the SNR center (as proposed by the previous work) may not be required to describe the overall dynamics of this SNR. Applying the Sedov-Taylor similarity solutions, we estimate the dynamical age of $\sim$17,000 yr and an explosion energy of $E_0 \sim 1.7 \times 10^{51}$ erg for B0049-73.6. We place a stringent upper limit of $L_X \sim 6.0 \times 10^{32}$ erg s^{-1} on the 0.3-7.0 keV band luminosity for the embedded compact stellar remnant at the center of B0049-73.6. Our tight estimate for the X-ray luminosity upper limit suggests that the compact stellar remnant of this SNR may be a similar object to those in a peculiar class of low-luminosity neutron stars (e.g., the so-called Dim Isolated neutron stars) or may possibly be a black hole.

Finally, we demonstrate our adaptive mesh grid method for the analysis of the rich SNR data. We developed our own computer software to implement this technique which is useful for an efficient spatially-resolved spectroscopic study of high-quality datasets of SNRs. As part of this software we also implement automated spectral

model fits for all individual spectra extracted from our adaptively defined small subregions. We illustrate the utility of this technique with an example study of SNR N63A in the LMC.

TABLE OF CONTENTS

LIST OF ILLUSTRATIONS

LIST OF TABLES

CHAPTER 1

INTRODUCTION

1.1 Stellar Evolution

In the deep interior of stars hydrogen nuclei undergo a series of nuclear fusion processes. In these nuclear reactions two or more atomic nuclei come close enough to form one or more different nuclei, releasing a large amount of energy due to the difference in mass between the products and reactants. Thus stars are thermonuclear furnaces in which lighter elements are fused (or "burned") into heavier nuclei by increasingly higher gas temperatures as the composition of the stellar core evolves.

Stars spend the majority of their lives on the so-called "main-sequence" stage, burning hydrogen into helium. When the star burns through its hydrogen supply, the star's core contracts. This core contraction triggers the burning of helium to create carbon and oxygen. Generally speaking, for stars with masses $\lesssim 8M_{\odot}$, this is the end of their nuclear fusion process. Stars of these masses lack sufficient gravity to generate core temperatures high enough to ignite carbon fusion. The core contracts until it is stopped by electron degeneracy pressure. The outer layers are ejected in the form of stellar winds leaving behind a hot core (typically consisting of C and O) the so-called white dwarf. However, if the star is massive enough (M $\gtrsim 8M_{\odot}$) it undergoes the core contraction until the pressure and temperature are sufficiently high to begin the next stage of the carbon fusion. As more advanced nuclear fusion progresses the stellar core becomes layered like onion-skins with progressively heavier atomic nuclei building up at the center (Figure 1.1). This process of progressive fusion continues

until an inert Fe-core is created, which marks the "ending phase" of a massive star's life.

1.2 Supernova

A supernova (SN) is the catastrophic explosion of a star at the end of its life. The specific properties of SNe are subject to many unique initial conditions, such as the stellar mass, different explosion mechanisms, explosion energies, and the structure of the surrounding circumstellar/interstellar material (CSM/ISM) to name a few, and thus their outcomes can vary wildly. The SN explosion is so energetic (typically with a kinetic energy of $\sim 10^{51}$ erg with an typical peak visual absolute magnitude (M_V) of $\sim$ -19.3 [Hillebrandt & Niemeyer 2000]) that it may briefly outshine the entire galaxy they inhabit and emit more energy than was created throughout the life of the star. The SN explosion ejects the stellar material out into space with velocities of $\sim$30,000 km s^{-1}.

SNe are categorized into two observational types (Type I and Type II) based on the presence of hydrogen (or lack thereof) in their optical spectrum (Type I having no hydrogen in their spectrum and Type II showing hydrogen). They are further subdivided into categories Ia, Ib, Ic, IIP, IIL, IIn, and IIb. Type Ia shows a strong ionized silicon line while Types Ib and Ic show no silicon absorption features in their spectrum. Type Ib show strong neutral helium lines while Type Ic lacks them. All Type II SNe show typical Type II spectra which is dominated by a broad hydrogen absorption line, and individual sub-types are classified based on the detailed shapes of the light curves and spectral line width (see Filippenko 1997 for more information on supernova classification.).

Core-collapse (CC) SNe are the result of an explosion of a massive star (M $\gtrsim$ $8M_{\odot}$), which may include Types Ib and Ic and all sub-classes of Type II. These massive

stars burn heavier elements (than He) which ultimately cause their demise. Once the star starts to produce Fe at the deepest core the fate of the star is sealed. Fe has the highest binding energy per nucleon of all the elements, meaning energy cannot be produced in the core by fusion of Fe. The process of burning Fe is endothermic and is a net-negative energy process (e.g., it takes more energy to fuse then is released). As the inert Fe core grows and eventually its mass becomes larger than the Chandrasekhar mass ($\sim 1.4 M_{\odot}$) its electron degeneracy pressure can no longer support the Fe-core against the force of gravity, and thus the Fe core catastrophically collapses while the rest of the star explodes as a SN.

The core-collapse SN explosion mechanism is not well understood. The conventionally agreed upon scenario is that the Fe core separates into two parts: a homologously collapsing inner core (i.e., $v \propto r$, where v is the speed of the in-falling material and r is the radius of the collapsing core) and a supersonically in-falling outer core. When the outer core reaches the inner core it elastically rebounds outward. The core-bounced material forms a shock wave propagating outward through the in-falling stellar material, which eventually explodes the star. The innermost Fe core collapses into either a neutron star or black hole, depending on its final mass. The debris of core-collapse SNe consist primarily of stellar ejecta, with the innermost ejecta consisting of explosive nucleosynthesis products (mostly Si-group elements with trace amounts of Fe). The nucleosynthesis yields of core collapse SNe are dominated by C, O, Ne and Mg, which are products of the various stellar burning phases during the stellar evolution (e.g. Woosley and Weaver, 1995; Thielemann et al., 1996; Chieffi and Limongi, 2004). The heavier Fe-group elements are mostly locked in the compact stellar remnant (neutron star or black hole).

Type Ia SNe are thought to be the result of thermonuclear runaway of a C/O white dwarf. When a C/O white dwarf exists in a close binary system it may accrete

material from its companion in either a single-degenerate (a nondegenerate companion star) or a double-degenerate (white dwarf companion star) channel. When the accreting (or merging) white dwarf's mass exceeds the Chandrasekhar mass ($\sim 1.4 M_{\odot}$) the star undergoes a thermonuclear runaway explosion unbinding the star. The detailed physics involved in these thermonuclear explosions and the nature of their progenitor systems are still debated (see Maoz et al. 2014 for a recent review). The explosion energy comes from thermonuclear fusion of C and O, rather than from gravitational energy during the collapse of a stellar core (as in core-collapse SNe). Unlike CC SN, Type Ia SN do not produce a stellar remnant (neutron star or black hole) at their centers, instead, they completely destroy the white dwarf.

1.3 Supernova Remnant

A supernova remnant (SNR) is the resulting structure from the explosion of a SN. SNRs are composed of the overabundant stellar debris and the blast wave from the SN explosion. SNRs provide insight into the explosion mechanisms of SNe as well as the galactic chemical evolution and star formation history of the galaxies they inhabit. Since a SNR is the remains of a SN explosion, SNRs contain direct imprints from nucleosynthesis yields and dynamics of the SN explosion. SNRs also allow us to probe their immediate surroundings via the blast wave shock front that sweeps-up and heats the surrounding ISM.

SNRs may evolve through three main phases starting with the so-called "free expansion" phase. In this phase of the SNR evolution, the swept-up ISM has little contribution to the overall dynamics of the system which are dominated by the kinetic energy of the SN explosion. As the blast wave ("forward shock") propagates outward, pressure drops behind the shock wave (McKee 1974) and the material interior to the forward shock cools adiabatically before the "reverse shock" forms and reheats

material in a "shell"-like region behind the forward shock (Reynolds 2008). This phase of SNR evolution may last for $\sim 10^3$ yr (the actual time period of this phase may depend on the ambient density structure into which the forward shock expands). Collisionless shocks at the outer boundary of the SNR may produce radiation with a featureless continuum spectrum from the shock-accelerated interstellar particles throughout the entire electromagnetic spectrum. In the X-ray band, this spectrum may be characterized by a power-law with photon index $\Gamma \sim 2.5$ which is attributed to synchrotron radiation from relativistically-accelerated electrons along the intensified interstellar magnetic fields in the post-shock gas (Reynolds & Chevalier 1981). The X-ray emission spectrum of such synchrotron radiations has been observed in young SNRs, particularly in the thin filamentary regions along their outermost boundaries (e.g., SN 1006 [Koyama et al. 1995]). The interior of the SNR is dominated by stellar material containing overabundant metal elements that were produced during the stellar evolution and SN explosion. This stellar material is heated by the reverse shock, whose X-ray spectrum is thermal and dominated by strong atomic emission lines from highly ionized metal elements. The forward- and reverse-shocked regions are separated by a boundary the so-called contact discontinuity (CD, see Figure 1.2 for a cartoon view of the overall SNR structure).

The second phase of the SNR evolution is known as the "Sedov phase", so named because the dynamical evolution of the blast wave (the forward shock) can be described by the Sedov-Taylor self-similar solution equations (Sedov 1959, see Equations 1.1, 1.2, and 1.3, where r is the radius of the spherical shock, E_0 is the initial explosion kinetic energy, ρ is the mass density of the surrounding material, t is the time since explosion, and v_{shock} is the velocity of the shock front).

$$r = E_0^{\frac{1}{5}} \rho^{-\frac{1}{5}} t^{\frac{2}{5}} \tag{1.1}$$

$$v_{shock} = \frac{dr}{dt} = \frac{2}{5} E_0^{\frac{1}{5}} \rho^{-\frac{1}{5}} t^{-\frac{3}{5}} = \frac{2}{5} \frac{r}{t} \tag{1.2}$$

$$E_0 = r^5 t^{-2} \rho \tag{1.3}$$

These Sedov solutions are simple 1-D calculations of the shock dynamics assuming an isotropic (spherically symmetric) expansion of the blast wave into a uniform density. The Sedov phase begins when the swept-up mass becomes comparable with that of the ejected material at the forward shock. During this phase the forward shock adiabatically expands and the shock expansion goes as $v_{shock} = 0.4r/t$. This phase may last for $\sim 10^{3-5}$ yr. The forward shock continues to sweep-up ISM until a significant amount of material has been accumulated that the blast wave begins to decelerate. This deceleration causes the reverse shock to turn over and propagate back towards the SNR center. For typical parameter values of a CC SN ($M = 10$–20 $M_\odot$, $E_0 = 10^{51}$ erg, and $n_0 = 1$ cm^{-3}, where M is the mass of the progenitor star, E_0 is the explosion energy, and n_0 is the pre-shock hydrogen density of the surrounding medium), the reverse shock will reach the center of the SNR in ∼7,000–13,000 yr (see equation 29 in Reynolds & Chevalier 1984). The X-ray emission from these middle aged SNRs may be described by a characteristic two-temperature thermal plasma (due to the superposition of the reverse-shock-heated stellar material (e.g., the metal-rich ejecta) and the forward-shock-heated swept-up ISM), typically with electron temperature $kT \sim 0.5$–2 keV (Borkowski et al. 2001), where k is the Boltzmann constant. The forward shock continues to propagate outward to form a dense shell of the swept-up interstellar gas. The reverse shock has now made significant progress toward the center of the SNR and might have heated a significant amount of the metal-rich ejecta gas.

The final phase of the SNR evolution is called the snowplow phase. In this phase of the SNR evolution the swept-up mass is significantly larger than the ejected H mass, thus the shock significantly slows and cools and radiative cooling becomes important. This phase may start $\sim 10^5$ yr after the explosion and would continue until the SNR cools off. Eventually the SNR is completely intermixed with the ISM. From this phase onward the SNR is of little interest to X-ray astronomy, as the SNR has mostly cooled below X-ray emitting temperatures and emit primarily in the optical and radio bands.

1.4 Utility of SNRs in the Magellanic Clouds

Generally, there are two observational restrictions that may affect our study of SNRs. The first is the ambiguity in distance scales to SNRs, which may affect our conclusions on the physical parameters (such as age, size, mass, energy, etc.) of the SNR. The second is the interstellar obscuration along the line-of-sight. Interstellar material obscures our vision by absorbing photons emitted from the SNR. Most Galactic SNRs are located along the Galactic plane where interstellar gas is concentrated and thus observations of SNRs in our Galaxy are heavily impacted by this interstellar extinction (except for those nearby).

As luck would have it, we can reduce the impact of these issues by utilizing SNRs located in a pair of the Milky Way's satellite galaxies, the Large and Small Magellanic Clouds (LMC and SMC, respectively). Distances to these galaxies (and thus to any objects in them) are well determined ($\sim$50 kpc for the LMC and 60 kpc for the SMC [Hilditch et al. 2005, Pietrzynski, G., et al. 2013]). These galaxies are projected at high latitudes ($b \sim -33^\circ$ for the LMC and $\sim -44^\circ$ for the SMC) off the Galactic plane. Therefore the Galactic interstellar obscuration is significantly lower along the line-of-sight toward the LMC and SMC ($N_{H,Gal} \sim 6\times10^{20}$ cm^{-2} towards the LMC and

$N_{H,Gal} \sim 4.5 \times 10^{20}$ cm^{-2} towards the SMC, Dickey & Lockman [1990], where N_H is the hydrogen column along the line-of-sight) compared to, for example, $N_{H,Gal} \sim 10^{22}$ cm^{-2} for Galactic SNRs on the far side of the Milky Way. Thus, observations of SNRs in the LMC and SMC are affected by considerably less interstellar extinction than those of Galactic SNRs, substantially increasing their *visibility*.

1.5 *Chandra* X-ray Observatory

The *Chandra* X-ray Observatory (*Chandra*, hereafter) is one of NASA's Great Observatories, and was launched on July 23, 1999 (Figure 1.3). *Chandra* utilizes a grazing incident optic (namely the High Resolution Mirror Assembly) that provides high angular resolutions ($\sim 0.5''$ on-axis) and a field of view of 1 degree (Weisskopf et al. 2003, see Figure 1.3 for a schematic view of the observatory). *Chandra* carries two primary focal plane instruments (Burke et al. 1997), the Advanced CCD Imaging Spectrometer (ACIS, Figure 1.4) and the High Resolution Camera (HRC). Both the HRC and ACIS have two separate arrays, an imaging array (HRC-I and ACIS-I) intended for wide field imaging and a spectroscopic array (HRC-S and ACIS-S) to be used in conjunction with transmission gratings that can be inserted into the optical path.

ACIS consists of 10 charge coupled devices (CCDs) arranged in two arrays (see Figure 1.4). One array consists of four CCDs in a 2×2 array (ACIS-I) with a field of view of $17' \times 17'$. The second array consists of 6 CCDs arranged in a 1×6 array (ACIS-S) to be used as a read-out for the High/Low Energy Transmission Grating (HETG and LETG, respectively). Two CCDs in the ACIS-S (S1 and S3) array are back-illuminated and have the gate electrodes facing away from the incoming photons, which gives them a greater quantum efficiency in the lower-energy band at photon

energies $E \lesssim 1$ keV. The remaining chips are front-illuminated which have slightly higher quantum efficiency in the higher-energy band. The ACIS detectors have the ability to perform imaging spectroscopy with no gratings in place. The combination of high spatial resolution ($\sim 0.5''$) and decent energy resolution ($\sim$95 eV at $E = 1.49$ keV) allows for detailed spectroscopic investigation of small features within large extended sources such as the SNRs that we analyze in this work. The *Chandra* ACIS provides the imaging spectroscopy with the highest spatial resolution (available with any existing X-ray telescope), which is required for the studies that we perform in this thesis. Thus, for this thesis we use the observation data acquired with ACIS. To date 56 SNRs have been detected in X-rays in the LMC (Maggi et al. 2016) and 23 SNRs have been detected in the SMC (Badenes et al. 2010) of which *Chandra* has observed 25 in the LMC and 7 in the SMC.

1.6 X-ray Data Analysis and Spectral Modeling

For the data processing and analysis we use the standard *Chandra* data analysis software package, the *Chandra* Interactive Analysis of Observations (CIAO)[1], as provided by the NASA *Chandra* X-ray Center. For spectral analysis we use the High Energy Astrophysics software suite (HEAsoft[2]) provided by the High Energy Astrophysics Science Archive Research Center (HEASARC) at NASA's Goddard Space Flight Center. Specifically we use the X-ray spectral analysis software XSPEC to analyze our observed spectra. For our fully-automated spectral extractions (see Chapter 4) we use the Interactive Spectral Interpretation System (ISIS[3]). ISIS provides full ac-

[1] http://cxc.harvard.edu/ciao/

[2] http://heasarc.nasa.gov/lheasoft/

[3] `http://space.mit.edu/cxc/isis/`

cess to all XSPEC models for X-ray spectral analysis, however, it also includes built-in support for parallel processing which drastically speeds up our spectral model fittings.

To analyze the observed X-ray spectrum of SNRs, we use an absorbed non-equilibrium ionization (NEI) plane-parallel shock spectral model (Borkowski et al. 2001) for radiations from an optically-thin plasma, which contains a number of atomic X-ray emission lines in a wide range of ionization states (i.e., VPSHOCK in XSPEC, based on the atomic data ATOMDB (Foster et al. 2012)). We use the recent NEI model (NEI version 2.0) which includes the prominent lines from H- and He-like ions as well as "inner-shell" lines from Li-like ions (these lines are important for under-ionized gas to correctly measure the electron temperature, see Badenes et al. 2006). This model also includes the latest Fe-L shell lines (prevailing at $E \sim 0.7$-1.2 keV, see Badenes et al. 2006). This model characterizes X-ray spectrum radiated by optically-thin hot gas with the following parameters; the electron temperature, the ionization timescale $n_e t$ (the multiplication of the electron density, n_e, by the time elapsed since the gas was shocked, t), and a normalization parameter which is the scaled volume emission measure (Equation 1.4, where n_H is the post-shock hydrogen number density, and V is the X-ray emitting volume).

$$EM = \int n_e n_H dV \tag{1.4}$$

The model parameters also include abundances for a number of elements (including C, N, O, Ne, Mg, Si, S, Fe, and Ni).

1.7 Thesis composition

This dissertation is comprised of three parts, an interstellar metallicity study of the LMC using X-ray emission from SNRs, a study of the detailed structure of an SNR in the SMC, and the description of our adaptive mesh grid methods to effectively

perform a detailed spatially-resolved spectral analysis of high-quality CCD data of SNRs (Note: this method was not used in the studies presented in Chapters 2 and 3. This method is intended for our future works on the detailed spatially-resolved spectral analysis of rich *Chandra* SNR data sets, which is beyond the scope of this thesis). In Chapter 2 we present an ISM composition investigation of the LMC using sixteen SNRs which we published in The Astronomical Journal (Schenck et al. 2016). In Chapter 3 we perform a detailed analysis of SNR B0049-73.6 in the SMC which we published in The Astrophysical Journal (Schenck et al. 2014). Finally, in Chapter 4 we describe the application of our adaptive mesh grid to systematically extract and analyze X-ray spectra from numerous small subregions throughout an SNR.

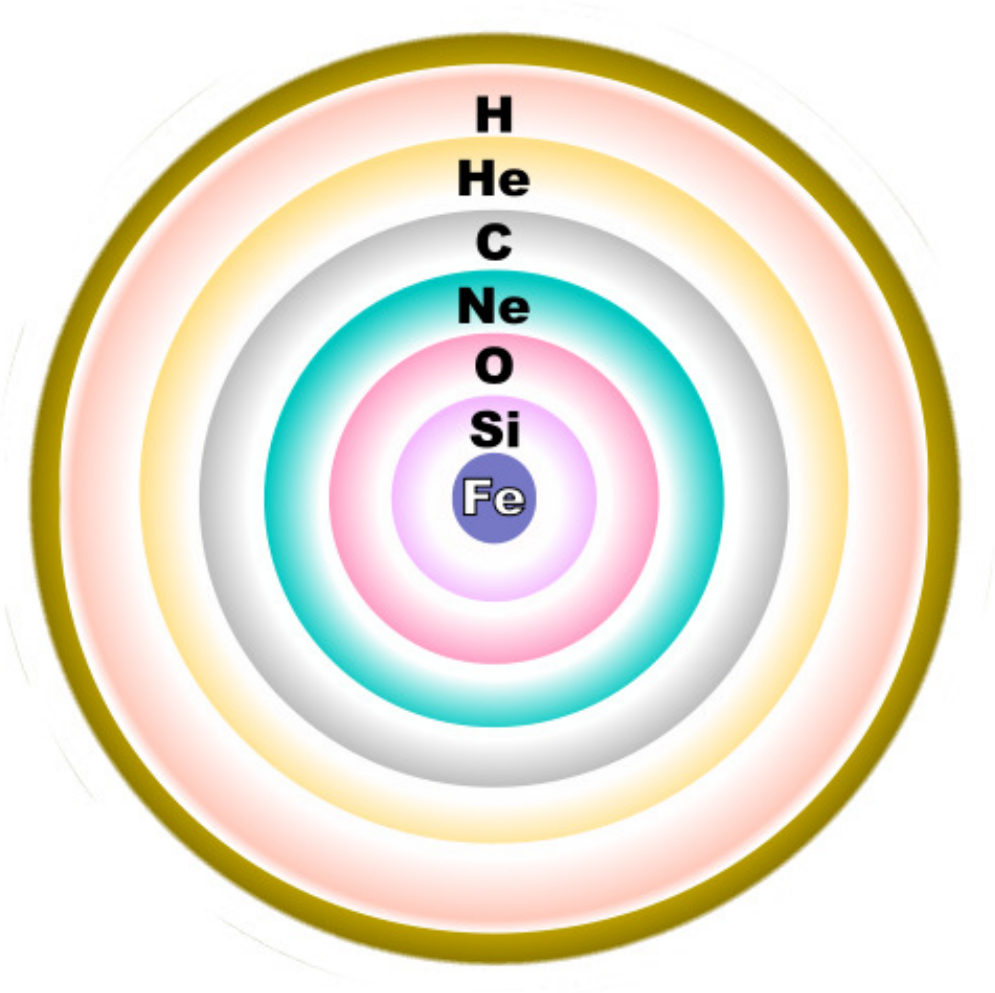

Figure 1.1 This diagram shows a cartoon-view of a cross-section of a massive, evolved star. In stars with $M \gtrsim 8M_{\odot}$, concentric shells of hydrogen, helium, carbon, neon/magnesium, oxygen, and silicon plasma are burned inside the star. The resulting fusion by-products rain down upon the next lower layer, building up the shell below. As a result of silicon fusion, an inert core of iron is steadily building up at the center. Image courtesy of R. J. Hall (`https://commons.wikimedia.org/wiki/File%3AEvolved_star_fusion_shells.svg`.

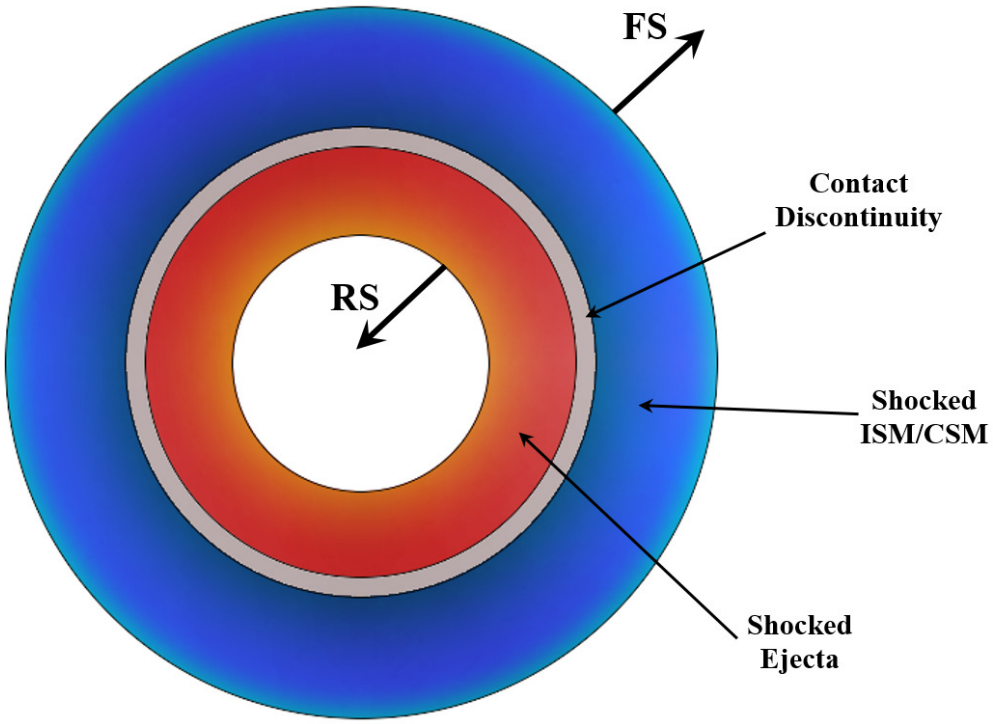

Figure 1.2 This diagram shows a cartoon-view of the basic structure (shock dynamics) of a SNR. The FS propagates radially outward away from the SNR center sweeping up and heating the ISM/CSM. While the RS propagates inward toward the SNR center heating the stellar ejecta. The FS and RS are separated by the CD. Image courtesy of Nicholas Berry (alby@4thcirclegames.com).

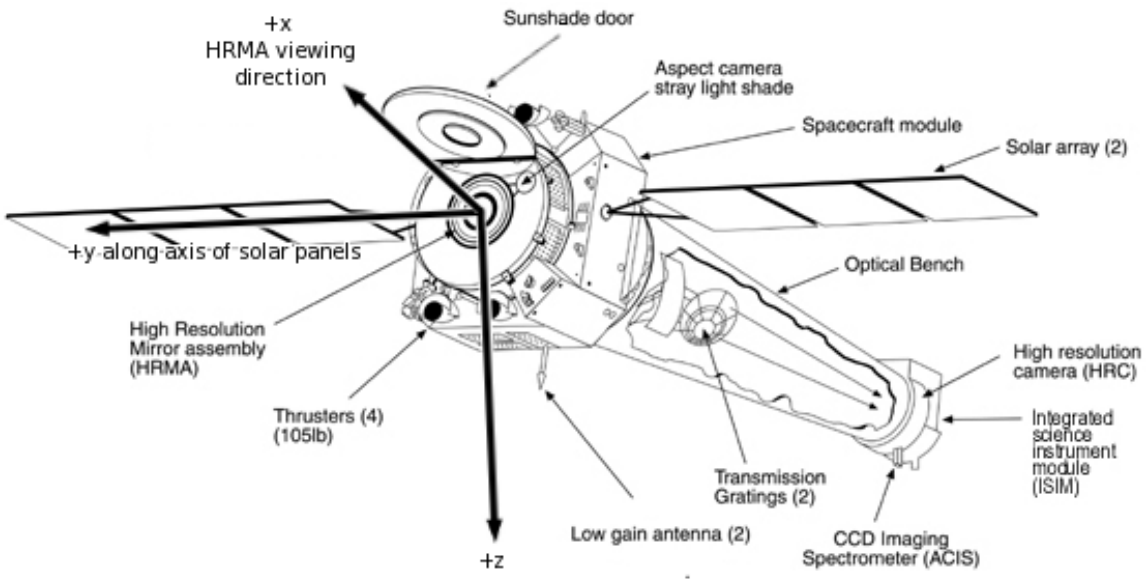

Figure 1.3 A schematic diagram of the *Chandra* X-ray Observatory. Credit: *Chandra* X-ray Center/*Chandra* Proposers Observatory Guide. Please see `http://cxc.harvard.edu/proposer/POG/html/index.html` for additional instrument information.

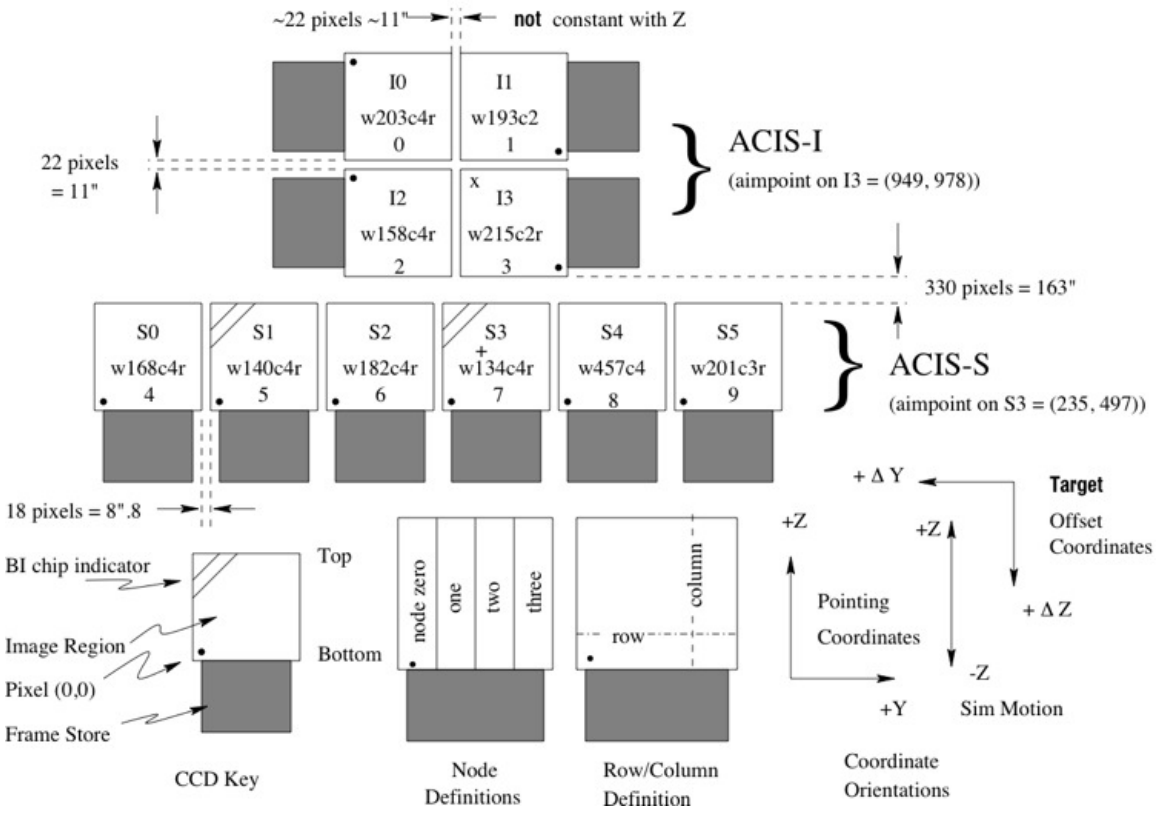

Figure 1.4 ACIS CCD layout, with default aimpoints shown for ACIS-I (shown with an 'X') and ACIS-S (shown with a '+') arrays. The ACIS-S3 and ACIS-S1 chips are back-illuminated; the rest are front-illuminated. Credit: CXC/*Chandra* Proposers Observatory Guide

CHAPTER 2

A *Chandra* Study of the Interstellar Metallicity in the Large Magellanic Cloud Using Supernova Remnants

2.1 Introduction

Measurements of the interstellar medium composition are essential for understanding galactic evolution and star-formation history. The LMC provides an excellent laboratory for the study of its ISM thanks to its proximity (∼50 kpc) and its low Galactic foreground absorption ($N_{H,Gal} \sim 6\times\ 10^{20}$ cm^{-2}, Dickey & Lockman 1990). SNRs are excellent probes of their surrounding ISM. The forward shock propagates through the ISM sweeping and heating it up. In young SNRs ($\lesssim 10^4$ yr) this swept-up ISM is hot enough to radiate in X-rays, allowing us to study interstellar metallicity based on X-ray observations. X-ray spectroscopy of SNRs to measure the metal abundances of gas-phase ISM was pioneered by Hughes et al. (1998, H98, hereafter) who utilized the integrated X-ray spectra of seven LMC SNRs, taken by *ASCA*. This method is independent of and complementary to the optical spectroscopy of stars and HII regions (e.g., Russell & Dopita 1992). With the high resolution imaging spectroscopy of modern *Chandra* data, we are now able to separate shocked ISM features from regions of metal-rich ejecta (e.g., Hughes et al. 2003,2006; Park et al. 2003a,2012; Borkowski et al. 2007). Thus, accurate measurements of the swept-up ISM abundances based on the high resolution *Chandra* data of the LMC SNRs are warranted.

We analyzed archival *Chandra* data of sixteen SNRs located in the LMC to estimate the ISM abundances of the LMC. Taking advantage of these high-resolution

Chandra data (angular resolution of $\sim 0.5''$ on axis, which is two orders of magnitude improvement from the *ASCA* data), we are able to effectively isolate the swept-up ISM from any metal-rich ejecta and/or pulsar wind nebulae (PWN) to make more realistic measurements of metal abundances in the LMC ISM. With our larger sample size we can also significantly reduce statistical uncertainties on the abundance measurements to help improve the accuracy of the LMC metallicity measurement. In the following subsections of Chapter 2, we present these results from our metal abundance measurements of the LMC ISM as we published in *The Astronomical Journal* (Schenck et al. 2016).

2.2 OBSERVATIONS & DATA REDUCTION

There are 59 detected SNRs in the LMC (Maggi et al. 2016), of which 56 SNRs have been observed in the X-ray band. 25 of them have been observed with *Chandra*, and those observational data are available in the public *Chandra* archive. We selected sixteen SNRs based on two criteria: (1) they show a well-defined swept-up ISM shell, and (2) they are relatively bright and/or observed with a long exposure time to allow us statistically significant measurements of elemental abundances in its swept-up shell. All of these sixteen SNRs were observed using the ACIS-S3. The archival *Chandra* data of these sixteen SNRs are comprised of thirty-four Observation IDs (ObsIDs, Table 2.1). Although there are a number of *Chandra* observations for SNR 1987A, we chose to exclude this remnant in our study. X-ray emission from SNR 1987A is dominated by shocked circumstellar material from the massive progenitor (Sonneborn et al. 1987), which may not represent the ambient LMC abundances. We processed these individual ObsIDs using CIAO version 4.3 (with the calibration database version 4.4) which includes corrections for the charge transfer inefficiency and the time-dependent contamination rate of the optical blocking filter.

The change in the contamination rate of the optical blocking filter in 2009 reduced the quantum efficiency of the ACIS by an additional ∼15% (which might have affected seven ObsIDs in our sample, in which the target SNRs were N49 and 0519-69.0). We then filtered these ACIS data following the standard data reduction procedure[1] which reprocesses the raw data by applying the latest calibration techniques and appropriate data filtering. There were periods of flaring particle background for observations of SNRs N63A and N49B. ObsID 777 (for the observation of N63A) had several short periods of high background (∼2 ks in total). ObsID 1041 (for the observation of N49B) had relatively high background for the last ∼4 ks out of the total ∼43 ks exposure. We removed these time periods from our analysis.

2.3 ANALYSIS & RESULTS

Here we describe our general approach to measure ISM abundances for each SNR selected in this study. First we created a 3-color map for each SNR (with the color codes of red: 300–700 eV, green: 700–1100 eV, and blue: 1100–7000 eV) to locate the areas of soft X-ray emission ("red" regions) presumably from the swept-up shell in its outermost boundary (Figure 2.1 and Figure 2.2). We verified our candidate swept-up ISM regions for individual SNRs in literature where available (see Section 2.4.4). We excluded regions for which X-ray emission from the shocked metal-rich ejecta has been reported in literature (see Section 2.4.4). Based on these criteria we selected several small and/or thin regions in the outermost boundary of each SNR (Figure 2.1 and Figure 2.2). We defined individual regions to extract at least ∼3,000 photon counts (in the 0.3–7 keV band) in each region to allow statistically significant spectral model fits. We binned each spectrum to contain a minimum of 20 counts per energy channel. We fit these candidate ISM spectra using an NEI plane-parallel

[1] `http://cxc.harvard.edu/ciao/guides/acis_data.html`

shock model (see Section 1.6) with two foreground absorption column components, one for the Galactic column ($N_{H,Gal}$) and the other for the LMC column ($N_{H,LMC}$). The absorbing column for the Galaxy was fixed at $N_{H,Gal} = 6.5 \times 10^{20}$ cm^{-2} for the direction toward the LMC (Dickey & Lockman 1990) while $N_{H,LMC}$ was allowed to vary. We characterized the background spectrum using the observed X-ray spectrum extracted from source-free regions just outside each SNR, and subtract it from the source spectrum to secure the background-subtracted source spectrum for each region. We fixed the redshift at $z = 286$ km s^{-1} for the LMC (McConnachie 2012).

In this work we intend to measure abundances for all metal elements whose atomic line emission was present in the spectra. In the 0.3–7.0 keV band our sample of SNR spectra typically shows atomic line emission features for both Heα and Lyα lines for O ($E \sim 0.57$ keV for Heα, $E \sim 0.65$ keV for Lyα), Ne ($E \sim 0.92$ keV for Heα, $E \sim 1.02$ keV for Lyα), Mg ($E \sim 1.35$ keV for Heα, $E \sim 1.47$ keV for Lyα), and Si ($E \sim 1.87$ keV for Heα, $E \sim 2.01$ keV for Lyα) as well as L-shell lines from Fe (present in the $\sim$0.70–1.10 keV band). Thus we fit the spectrum of each region in individual SNRs with the abundance values for O, Ne, Mg, Si, and Fe varied (hereafter, all elemental abundances are with respect to solar values [Anders & Grevesse 1989]). We found no significant variations of our estimated ISM abundances and electron temperature among the sub-regions within each individual SNR. We then averaged these measured abundance values for each SNR and summarize them in Table 2.2. We constrain the mean elemental abundances for each SNR within $\sim$20% (uncertainties are with 90% confidence, hereafter). Representing the mean interstellar abundances of the LMC, our average measured elemental abundances estimated from all sixteen SNRs, as listed in Table 2.2, are significantly lower (by a factor of $\sim$2 except for Si) than those measured by H98 (see Figure 2.3 for comparisons of the seven SNRs shared by both studies).

2.4 DISCUSSION

2.4.1 Comparisons with Previous *ASCA* Measurements

H98 used *ASCA* data of seven bright LMC SNRs (N23, N49, N49B, N63A, DEM L71, N132D, and 0453-68.5) to estimate the elemental abundances of O, Ne, Mg, Si, S, and Fe in the LMC. Comparisons of the elemental abundances of the LMC ISM between this work and H98 are shown in Figure 2.3. Except for Si our measured elemental abundances are generally lower than H98 by a factor of $\sim$2. We identify several contributors to the discrepancy between H98 and our work. First, due to the large point spread function of the *ASCA* detectors ($\sim 2'$ half power diameter), H98 analyzed the X-ray spectrum integrated over each entire SNR, while we used spectra extracted from resolved swept-up ISM features in each SNR. It has been well documented that N49, N49B, DEM L71 and N132D contain emission from metal-rich ejecta both in their central regions and in some cases even out near the outermost edges (Hughes et al. 2003; Park et al. 2003a, 2012; Borkowski et al. 2007).

N49B contains Mg-rich ejecta in an extensive area in the SNR center (Park et al. 2003a). In fact, although statistical uncertainties are relatively large, H98 measured a higher Mg abundance ($\sim$50% higher) for N49B than in other SNRs in their sample (see Figure 2.3). DEM L71 contains an Fe-rich central ejecta nebula (Hughes et al. 2003), and H98 measured a higher Fe abundance in DEM L71 than in the other SNRs in their sample ($\sim$50% higher, see Figure 2.3). N49 contains Si- and S-rich ejecta regions in its interior and in an "ejecta bullet" feature in the southwestern boundary (Park et al. 2012). N132D shows enhanced O abundance throughout its interior (Borkowski et al. 2007). We excluded these ejecta-dominated regions in our abundance measurements. Any embedded pulsar and/or PWN might also have affected abundance measurements in the *ASCA* data. N49 is coincident

with an X-ray counterpart of a soft Gamma-ray repeater (SGR 0526-66; e.g., Park et al. 2012) while 0435-68.5 contains a PWN (e.g., McEntaffer et al. 2012). The continuum-dominated emission from these pulsar and/or PWN might have resulted in underestimates of abundances when the integrated SNR spectrum was used to measure them.

To investigate the effect from metal-rich ejecta on ISM abundance measurements we have taken two regions from DEM L71 (one ISM region [the yellow region in Figure 2.4] and one metal-rich ejecta region [red region in Figure 2.4]) with similar photon statistics. We performed spectral model fits for the ISM region, the metal-rich ejecta region, and the combined ISM + metal-rich ejecta region (Figure 2.4). We fixed in our measured ISM abundances for DEM L71 (see Table 2.2) into each spectral model, and allowed the electron temperature, ionization timescale, and normalization to vary. The fit was statistically acceptable for the ISM region ($\chi^2_\nu = 1.01$). The fit was statistically unacceptable for the metal-rich ejecta region ($\chi^2_\nu = 7.0$) and the fit was also statistically unacceptable for the combined spectrum ($\chi^2_\nu = 2.85$). We then re-fit the three spectra allowing the elemental abundances for O, Ne, Mg, Si, and Fe to vary, and found statistically acceptable fits for all three spectra (ISM $\chi^2_\nu = 1.0$, Ejecta $\chi^2_\nu = 1.1$, ISM+Ejecta $\chi^2_\nu = 1.1$). For the ISM-only spectra we found metal abundances similar (within $\sim$10% uncertainties) to our measurements for DEM L71 shown in Table 2.2. For the metal-rich ejecta region we found significantly enhanced abundances compared to those for the ISM-only region: the Si and Fe abundances are higher than the ISM-only values by a factor of $\sim$2 and an order of magnitude, respectively. For the combined spectra, as perhaps expected, we estimated moderately enhanced abundances compared to the ISM-only abundances: i.e., the Ne and Fe abundances are higher than the ISM-only values by a factor of $\sim$2, and the Si abundances is $\sim$20% higher than the ISM-only value. We note that these moder-

ately enhanced abundances in the combined spectrum are in good agreement with those measured by H98 for DEM L71. Our test analysis of N49, N49B, and N132D shows similar results, confirming that the contamination from the overabundant stellar ejecta gas in the integrated SNR spectra is in part responsible for the discrepancy between the LMC abundance measurements of H98 and this work.

Similarly we show the effect of PWN on ISM abundance measurements. We selected one ISM region (the green region in Figure 2.5) and one region from the PWN (the red region in Figure 2.5) in SNR 0453-68.5 with similar photon statistics. We performed spectral model fits for the ISM region, PWN region, and the combined ISM + PWN region (Figure 2.5). We fixed in our measured ISM abundances for 0453-68.5 (Table 2.2) into each spectral model, and only allowed the electron temperature, ionization timescale, and normalization to vary. The fit was statistically acceptable for the ISM-only region ($\chi^2_\nu = 1.1$ in the $0.3-2.0$ keV band). The fit was statistically unacceptable for the PWN region ($\chi^2_\nu = 2.5$ in the $0.3-5.0$ keV band) as well as the ISM+PWN region ($\chi^2_\nu = 2.9$ in the $0.3-5.0$ keV band). We then re-fit all spectra allowing the elemental abundances to vary. We found statistically acceptable fits for each individual spectrum (ISM $\chi^2_\nu = 1.1$, PWN $\chi^2_\nu = 1.3$, and ISM+PWN $\chi^2_\nu = 1.4$). For the ISM-only region we measured metal abundances similar (within $\sim$10% uncertainties) to our measurements for 0453-68.5 as shown in Table 2.2. For the PWN region we found somewhat lower abundances ($\lesssim$0.1 solar) compared to those in the ISM-only regions (Table 2.2). For the ISM+PWN region we also found somewhat lower abundances ($\lesssim$0.1 solar) compared to those in the ISM-only regions (Table 2.2). H98 indeed found $\sim$10–50% lower Ne, Mg, and Si abundances compared to the rest of the SNRs in their sample, and they interpreted that the lower mean abundance for this remnant is due to less contamination by metal-rich ejecta (see Figure 5 in H98).

To test the spectral model dependence of abundance measurements between H98 and this work we fit the *ASCA* data of the seven SNRs (used in H98) with the NEI plane-shock model used in this work. Based on our plane-shock model fits of *ASCA* data, we measured the elemental abundances of O, Ne, Mg, Si, and Fe (Figure 2.6). Our abundance measurements for Ne and Fe are consistent with those by H98, while our O, Mg, and Si abundances are somewhat different than those by H98 (Figure 2.6). This suggests that the discrepancy in the abundance measurements for O, Mg, and Si between H98 and this work is in part due to the use of different spectral models (e.g., H98 used a different set of atomic data and NEI model codes than those used in this work). Also, we fit the integrated *Chandra* spectra (extracted from each of the seven SNRs) with our NEI plane-shock model, and measured the elemental abundances of O, Ne, Mg, Si, and Fe (Figure 2.6). Abundance measurements are generally consistent between these *Chandra* and *ASCA* plane-shock model fits, whereas the Fe abundance is somewhat lower in our *Chandra* measurement. These results suggest that, in addition to the ejecta effect, there appears to be a model-dependence in abundance measurements as well as some systematic uncertainties between *Chandra* ACIS and *ASCA* data (probably at a less-significant level).

Finally, we note that the *Chandra* ACIS-S3 detector is significantly more sensitive than that of the *ASCA* detectors with a $\sim$three times larger effective area at $E \lesssim 1$ keV. Considering that O, Ne, and some Fe-L emission lines are located at photon energies below 1 keV, measuring abundances for those elements based on *Chandra* data would be generally more advantageous.

2.4.2 Comments on Spatial Variation of LMC Abundances

We explore variations of our measured ISM abundances across the LMC (see Figure 2.7 for each SNR's location across the face of the LMC). We first investigate any

spatial variation of our measured LMC abundances depending on SNR types (Type Ia vs CC) with which we measured their "local" ISM abundances. In our sample we have ten CC SNRs, five Type Ia SNRs, and one un-typed SNR (Table 2.2). We find no significant variation in elemental abundances for Ne, Mg, Si, or Fe among these different types of SNRs (Figure 2.8). The O abundance appears to show a marginal enhancement for N63A, N49, and N49B (the best-fit values are $\sim$50% higher than those for the rest of the SNRs in our sample, but with large uncertainties). All of these three SNRs are located near the northern boundary of the LMC (Figure 2.7). Possibly, this part of the LMC may contain O-enhanced environments than the rest of the LMC.

We also explore variations of ISM abundances between star-forming (SF) and non-star-forming (NSF) environments. In our sample there are ten SNRs located in known star-forming regions while the remaining six SNRs are located in non-star-forming regions (see Figure 2.7). For Ne, Mg, and Si there is no significant abundance variations between SNRs in either environment. The O abundance shows marginal evidence of enhancements in star-forming environments (Figure 2.9). This is likely due to the moderate enhancement of the O abundance in N63A, N49, and N49B (Figure 2.8), all of which are located in star-forming regions near the northern boundary of the LMC. We note that the 30 Dor region (the largest active star-forming region in the LMC) does not show evidence for an O-enhancement compared to the other parts of the LMC. Thus, if the O enhancement in the northern boundary of the LMC is true, it may not necessarily be related with the star-forming activity, and its origin is unclear. It is also worth mentioning that the Fe abundance appears to be marginally enhanced in the non-star-forming regions. However, this suggestive Fe-enhancement is not conclusive in the current data due to relatively large uncertainties, and thus it is difficult for us to further discuss it.

2.4.3 Comparisons With Other LMC Abundance Measurements

Recent optical measurements of elemental abundances in the LMC use large samples of field stars (Cole et al. 2005; Pompia et al. 2008; Lapenna et al. 2012; Van der Swaelmen et al. 2013) to measure the elemental abundances of O, Mg, Si, and Fe as well as much heavier elements. Lapenna et al. (2012)'s O, Mg, and Si abundances are all consistent with our abundance measurements (Figure 2.10). Lapenna et al. (2012) showed that metallicity distributions tend to peak at about -0.57 dex for most field star samples; e.g., [Fe/H] = 6.9 (where [X/H] = 12 + log[X/H], with X referring to the number density of the element being estimated and H is the number density of hydrogen). This is in general agreement (within ∼10%) with our measurement of [Fe/H] = $6.84^{+0.03}_{-0.02}$. Also, our results are in good agreement with those by Korn et al. (2000) for Mg and Si (Figure 2.10). On the other hand there is discrepancy between our LMC abundance measurements and some other works: e.g, our measured abundances (with an exception of Si) are generally lower than those measured by Russell and Dopita (1992) by a factor of ∼2–3. The origins of this discrepancy are unclear. Possibly there are systematic differences between measuring the ISM abundances using different objects at different wavelengths (e.g., SNRs vs HII regions and/or stars).

Recently Maggi et al. (2016) performed an X-ray study of 51 SNRs in the LMC utilizing data obtained with *XMM-Newton* Observatory. They detected metal-rich ejecta in a large portion of their sample (39 out of 51 SNRs). The remaining twelve SNRs were assumed to be dominated by swept-up ISM emission. They used the integrated spectrum from each individual SNR to measure the ISM abundance of the LMC. To increase their sample size they included SNRs (among the ejecta-dominated SNRs) that showed ISM-like abundances for at least one element. Then, they measured the LMC abundances for O, Ne, Mg, Si, and Fe. Their measurements ([O/H]

$= 8.01^{+0.14}_{-0.21}$, [Ne/H] $= 7.39^{+0.11}_{-0.15}$, [Mg/H] $= 6.92^{+0.20}_{-0.37}$, [Si/H] $= 7.11^{+0.20}_{-0.40}$, and [Fe/H] $= 6.97^{+0.13}_{-0.18}$) are generally consistent with our measured elemental abundances (Figure 2.10). We note that Maggi et al's results are based on the integrated spectrum from each SNR (due to the poor angular resolution of the *XMM-Newton* detectors) rather than the spatially-resolved spectroscopy used in our study. Also, statistical uncertainties on their ISM abundance estimates are significantly larger than those on our measurements typically by a factor of ∼3–4. While LMC abundance measurements are generally consistent between Maggie et al. (2016) and this work, we conclude that our results based on the high resolution *Chandra* data represent more accurate estimates of the LMC abundances.

2.4.4 Summary for Individual SNRs

2.4.4.1 0453-68.5

0453-68.5 is a faint, aged (>17,000 yr old), SNR showing a clear limb-brightened shell that is dominated by X-ray emission from the swept-up ISM (McEntaffer et al. 2012). 0453-68.5 contains a PWN at its center solidifying its classification as a CC explosion (Gaensler et al. 2003; McEntaffer et al. 2012). We selected six regions from around the outer swept-up shell, as shown in Figure 2.1a, to estimate abundances for O, Ne, Mg, and Fe. Our abundance measurements from these six sub-regions are all consistent within statistical uncertainties, and thus we summarize the average abundances in Table 2.2. We were unable to constrain the Si and S abundances in 0453-68.5 because of the spectrally-soft nature of the X-ray emission (photon statistics are poor at $E > 1.5$ keV). McEntaffer et al. (2012) studied several regions partially overlapping with the regions used in this work. Their measured O abundance (O $= 0.17 \pm 0.02$) is significantly lower compared to Russell & Dopita (1992) value

(O = 0.263) but is consistent with H98's measurement within uncertainties (O = 0.21 ± 0.05). Our measured value for the O abundance (O = 0.08 ± 0.01) is lower than that by H98. We note that McEntaffer et al. (2012) allowed only the O abundance to vary in their spectral model fits while fixing all other abundances at the LMC values by Russell and Dopita (1992). Thus, their O abundance measurement might have been affected by those fixed abundance values for other elements.

2.4.4.2 DEM L71

DEM L71 shows a double-shock morphology consisting of an outer swept-up ISM shell surrounding a central bright region of reverse-shock heated ejecta (Hughes et al. 2003). The composition of the metal-rich ejecta shows enhanced Si and Fe abundances, with a lack of O, classifying it as a Type Ia SNR (Hughes et al. 2003). We measured the elemental abundances for O, Ne, Mg, Si, and Fe based on spectra extracted from seven regions along the outer swept-up shell (Figure 2.1b). The measured elemental abundances are consistent among all these seven sub-regions, and the averaged abundance values are shown in Table 2.2. Our measured elemental abundances are generally in agreement with those found in the inner rim region of the swept-up shell by Hughes et al. (2003).

2.4.4.3 N23

N23 is an irregular shaped SNR which appears to originate from a CC explosion of a massive star (Hughes et al. 2006). N23 shows a compact object near its center. This compact source is probably the stellar remnant from the explosion of a massive star, although its association with the SNR is still under debate (Hughes et al. 2006, Hayato et al. 2006). Hughes et al. (2006) found that most of the emission from N23 shows LMC-like elemental abundances, and found only one region (located near

the center of the remnant, west of the compact object) with enhanced elemental abundances (∼2-3 × LMC abundances). We selected four regions from all around the outer boundary of the SNR (Figure 2.1c, avoiding the metal-rich region found by Hughes et al. 2006) and measured the elemental abundances for O, Ne, Mg, Si and Fe. The measured elemental abundances are consistent among the four sub-regions. We present the average values for our measured abundances in Table 2.2. Our measured ISM abundance values are in good agreement with those in the east rim estimated by Hughes et al. (2006).

2.4.4.4 0519-69.0

0519-69.0 has been classified as a Type Ia SNR by Hughes et al. (1995). They found that 0519-69.0 is an O-poor SNR with Fe-rich ejecta throughout its central regions. 0519-69.0 shows a clumpy morphology with a clear inner ejecta nebula surrounded by a thin shell of swept-up ISM (Kosenko et al. 2010). We selected four thin red regions (dominated by spectrally soft X-ray emission) along the outermost boundary of the SNR (Figure 2.1d) to measure the elemental abundances for O, Ne, Mg, Si, and Fe. The measured elemental abundances are consistent among all four sub-regions. The averaged abundances are shown in Table 2.2. Abundance measurements from this outer swept-up shell of 0519-69.0 have not been previously reported in literature.

2.4.4.5 N49B

N49B shows Mg- and Si-rich ejecta near its center (Park et al. 2003a). N49B shows bright circumferential filaments that are emission from dense shocked ISM. We selected six regions along the outermost boundary (Figure 2.1e). We measured the elemental abundances for O, Ne, Mg, Si and Fe. Our measured elemental abundances

are consistent among all six sub-regions, and the average abundance values are shown in Table 2.2. Our measured abundances are in agreement with those measured in the bright southern swept-up shell by Park et al. (2003a).

2.4.4.6 N132D

N132D is the brightest SNR in the LMC and belongs to the rare class of O-rich SNR. Optical observations have shown high-velocity O-rich ejecta, indicating a CC origin for this SNR (Morse, Winkler, & Kirshner 1995). N132D interacts with CO clouds located all around the SNR supporting its CC origin (Banas et al. 1997; Sano et al. 2015). N132D shows a complicated filamentary morphology in X-rays with moderately enhanced metal-rich ejecta in its central regions (Borkowski et al. 2007). We measured the elemental abundances of O, Ne, Mg, Si and Fe based on spectra extracted from eight sub-regions from the outermost boundary (Figure 2.1f) and bright central filaments of the shocked ISM. The measured abundances are consistent among these eight sub-regions, and we present average abundance values in Table 2.2. We note that in their ejecta spectral analysis Borkowski et al. (2007) assumed 0.4 solar abundances for the underlying emission component originating from the swept-up medium.

2.4.4.7 N49

A soft Gamma-ray repeater (SGR 0526-66), a rare class of highly-magnetized neutron stars, is projected within the boundary of N49 (Cline et al. 1982; Rothschild et al. 1994), suggesting a CC origin for N49, although the physical association between SGR 0526-66 and N49 is unclear (Gaensler et al. 2001; Klose et al. 2004; Badenes et al. 2009; Park et al. 2012). N49 shows some regions of Si- and S-rich ejecta (including an ejecta "bullet" in the southwest boundary [Park et al. 2012]). N49 is

also interacting with clumpy molecular clouds (Vancura et al. 1992) in the eastern and southeastern regions giving rise to complicated spectral nature of X-ray emission in that area (Park et al. 2003b). Avoiding these ejecta features and regions where the shock is interacting with clumpy molecular clouds, we selected two regions from the outermost boundary in the southern rim of the SNR (Figure 2.1g). Our measured abundances are consistent between the two selected regions, and are also in agreement with those measured by Park et al. (2012). We measured the elemental abundances for O, Ne, Mg, Si and Fe, and the average abundance values are shown in Table 2.2.

2.4.4.8 N206

N206 is a mixed-morphology SNR (Williams et al. 2005) with a bright eastern band surrounded by a diffuse swept-up ISM shell. N206 is suggested to be a CC SNR based on observed ejecta elemental abundance structure (Williams et al. 2005). We selected two regions from the diffuse ISM shell (Figure 2.1h) and measured the O, Ne, Mg, Si and Fe abundances. The elemental abundances were consistent between these two sub-regions. The average abundance values are shown in Table 2.2. We note that our measured abundances are lower (by a factor of $\sim$2 for O, Ne, Mg and Fe) than those estimated by Williams et al. (2005) while our Si abundance value is similar to that estimated by Williams et al. (2005). This discrepancy appears to be due to the metal-rich ejecta contamination in the ISM abundance measurements in Williams et al. (2005) from an ejecta feature in the western part of their ISM shell region.

2.4.4.9 0534-69.9 and 0548-70.4

0534-69.9 and 0548-70.4 show a bright central metal-rich ejecta nebula surrounded by a limb-brightened swept-up ISM shell (Hendrick et al. 2003). Based on

low O/Fe abundance ratios in the central ejecta regions of both SNRs Hendrick et al. (2003) classified them as Type Ia explosions. In these SNRs the swept-up ISM emission can be clearly separated from the central ejecta emission. We extracted X-ray spectra from two outer boundary regions of 0534-69.9 (Figure 2.2i) to measure the elemental abundances for O, Ne, Mg, Si and Fe. We selected four regions in the outermost shell for 0548-70.4 (Figure 2.2p) and measured the elemental abundances for O, Ne, Mg, and Fe. The measured elemental abundances are consistent in all sub-regions in each SNR. The averaged elemental abundances for these SNRs are shown in Table 2.2. There are no previous estimates of metal abundances in the swept-up shell in these SNRs in literature.

2.4.4.10 DEM L238

DEM L238 is characterized by a bright central emission surrounded by limb-brightened swept-up ISM emission to the north, east, and west. The bright central emission shows enhanced Fe abundance suggesting that DEM L238 is a Type Ia SNR (Borkowski et al. 2006a). We selected two regions from the outer shell to measure the elemental abundances for O, Ne, Mg and Fe (Figure 2.2j). The measured elemental abundances from both regions are consistent with each other. The average elemental abundances are shown in Table 2.2. There are no previous measurements of the abundances in the swept-up shell in DEM L238.

2.4.4.11 N63A

N63A is the second brightest SNR in the LMC and is embedded in an HII region with its position coincident with the OB association NGC 2030 (Warren et al. 2003). This suggests a massive Population I progenitor for N63A (Chu & Kennicutt 1988). N63A shows many interesting morphological features such as “loops” and “plumes” at

the outermost boundary of the SNR along with many filamentary features throughout the SNR. The loop and plume features appear to show LMC-like abundances (Warren et al. 2003). However, we exclude these regions from our ISM study since their origin (shocked ISM vs ejecta) is unclear (Warren et al. 2003). Warren et al. (2003) showed that the column density toward N63A varies across the SNR. We selected seventeen regions in N63A from all around the outermost boundary (Figure 2.2k). These regions show similar column densities to one another (as shown in Warren et al. 2003). Initially we fitted these seventeen sub-regional spectra with the column density varied. The measured column densities are all consistent within statistical uncertainties, and thus we repeated our spectral model fits for all of these sub-regions with $N_{H,LMC}$ fixed at the mean value ($N_{H,LMC} = 1.1 \times 10^{21}$ cm^{-2}). We measured the elemental abundances for O, Ne, Mg, Si and Fe (Table 2.2). Our elemental abundances are in good agreement with those found by Warren et al. (2003).

2.4.4.12 Honeycomb Nebula

The Honeycomb nebula is a peculiar SNR. Its name is due to its optical morphology consisting of over 10 loops (with sizes of ∼2–3 pc) created by a SN blast wave interacting with sheets of dense but porous interstellar gas (Chu et al. 1995). As shown in Figure 2.2l, Honeycomb's overall morphology is unlike most SNRs who show a coherent shell-like structure. We probed Honeycomb for possible metal-rich ejecta and found no evidence of enhanced elemental abundances. We identified an X-ray point source located within the southwestern limb as a CXOXASSIST source (X053543.01-691817.5). We found that the X-ray spectrum of this point source can be equally fitted by several different models because of the poor photon statistics (240 counts in the 0.5-7 keV band): e.g., a power law (photon index $\Gamma \sim 1.9$, $N_{H,LMC}$ $\sim 7 \times 10^{20}$ cm^{-2} with $\chi^2_\nu = 0.7$), a blackbody (kT ~ 0.6 keV, $N_{H,LMC} \sim 2 \times 10^{20}$

cm^{-2} with $\chi^2_\nu = 1.4$), and a plane shock (kT $\sim$ 8 keV, $N_{H,LMC} \sim 5 \times 10^{20}$ cm^{-2} with $\chi^2_\nu = 1.1$). We note that the best-fit electron temperature for the plane shock model is extremely high and it is unlikely adequate for this point source. This suggests either a power law or blackbody model would be appropriate to describe the observed X-ray spectrum of this source. The best-fit column for the blackbody model ($N_{H,LMC} \sim 2 \times 10^{20}$ cm^{-2}) favors this source's physical association with the Honeycomb nebula, while the column implied for the best-fit power law model ($N_{H,LMC} \sim 7 \times 10^{20}$ cm^{-2}) is considerably larger than that for the Honeycomb nebula ($N_{H,LMC} \sim 2 \times 10^{20}$ cm^{-2}). However, the uncertainties on the column measurements for this point source in these models are large due to poor photon count statistics. Deeper observations are required to reveal the true nature of this X-ray point source. We extracted two spectra from Honeycomb to measure the ISM abundances (Figure 2.2l). One regional spectrum was extracted from the entire northeastern limb and the other regional spectrum was extracted from the entire southwestern limb (excluding the X-ray point source). We measured the elemental abundances for O, Ne, Mg, and Fe (Table 2.2). There are no previous ISM abundance measurements for this SNR in literature.

2.4.4.13 N157B

N157B contains one of the most energetic pulsars known (PSR J053747.39–691020.2). This pulsar is surrounded by a bright non-thermal X-ray nebula which likely represents a toroidal pulsar wind terminal shock observed edge-on (Chen et al. 2006). While N157B shows metal-rich ejecta through its interior close to the pulsar, diffuse swept-up ISM emission extends significantly to the north (Chen et al. 2006). We used a northeastern region to measure the elemental abundances of O, Ne, Mg

and Fe (Figure 2.2m). Our measured elemental abundances are shown in Table 2.2. There are no previous abundance measurements for the swept-up shell in this SNR.

2.4.4.14 0540-69.3

0540-69.3 has been identified as one of a handful of O-rich SNR in the LMC, and it contains a bright pulsar and PWN which have been throughly studied at many different wavelengths (e.g., Middleditch & Pennypacker 1985; Manchester et al. 1993a, 1993b; Gotthelf & Wang 2000; Kaaret et al. 2001; Petre et al. 2007). These O-rich ejecta and central pulsar solidify its CC origin. 0540-69.3 contains non-thermal emission in the form of "arcs" in the eastern and western boundaries of the SNR, which are suggestive of efficient cosmic-ray acceleration in the SNR shock (Park et al. 2010). Park et al. (2010) detected candidate metal-rich ejecta regions in the southern part of the SNR. We extracted spectrum from two regions in the western boundary of the SNR avoiding these PWN, non-thermal arcs, and candidate ejecta regions (Figure 2.2n). We measured the elemental abundances for O, Ne, Mg, Si, and Fe. Our measured elemental abundances are consistent between both regions and the average values are shown in Table 2.2. Hwang et al. (2001) fixed elemental abundances at the LMC values by Russell and Dopita (1992) in their spectral model fit for their ambient medium region. However, their overall model fits are statistically poor ($\chi^2_\nu = 1.7 - 2.5$). They noted that their measurements might have been contaminated by metal-rich ejecta.

2.4.4.15 DEM L316B

DEM L316B is a faint SNR that shows several central knots surrounded by diffuse shell-like emission. DEM L316B has been typed as a CC SNR based on the observed ejecta abundance ratios (Williams & Chu 2005). Avoiding metal-rich ejecta

features throughout DEM L316B's center we extracted the X-ray spectrum from a shell region surrounding the entire SNR (Figure 2.2o) to measure the ISM elemental abundances for O, Ne, Mg, Si and Fe. Our swept-up shell region is similar to Region 12 in Williams & Chu (2005). We are unable to compare our elemental abundance values to those found by Williams & Chu (2005) since they did not exclusively provide the abundance values for Region 12. We note that Williams & Chu (2005) did find significantly under-abundant Fe (Fe $\sim 0.10 \pm 0.03$) in some regions of DEM L316B, which is consistent with our measurement of the Fe abundances in this SNR.

2.5 Summary

Using the high resolution archival *Chandra* ACIS data of sixteen SNRs in the LMC we measure the elemental abundances of O, Ne, Mg, Si and Fe of the gas-phase ISM in the LMC in an unprecedented precision in X-rays. For our spectral extractions we avoid any contamination from metal-rich ejecta and/or PWN. We find lower elemental abundances (by a factor of $\sim$2 for all elements except for Si) for the ISM in the LMC compared to those found by H98 who similarly used SNRs in the LMC (based on *ASCA* data). We attribute this discrepancy to several effects such as the overabundant metal-rich ejecta contamination in the *ASCA* measurements and spectral model-dependence of the abundance measurements between H98 and this work. There also appear to be some systematic uncertainties in the elemental abundance measurements between two different instruments (*Chandra* vs *ASCA*).

We find no significant variation of ISM abundances within individual remnants or between SNR types. The O and Fe abundances appear to show marginal evidence for variation between star-forming and non star-formation environments. To confirm or dispute this suggested spatial variation of abundances, deeper observational data with a larger sample may be required. We compared our results with optical mea-

surements of LMC abundances in literature and found agreements with some recent results (e.g., Korn et al. 2000; Lapenna et al. 2012), however, our measurements do not agree with some published optical measurements. Our LMC abundance measurements are generally consistent with recent *XMM-Newton* results (Maggi et al. 2016), although the *XMM-Newton* results involve larger uncertainties than those on our measurements.

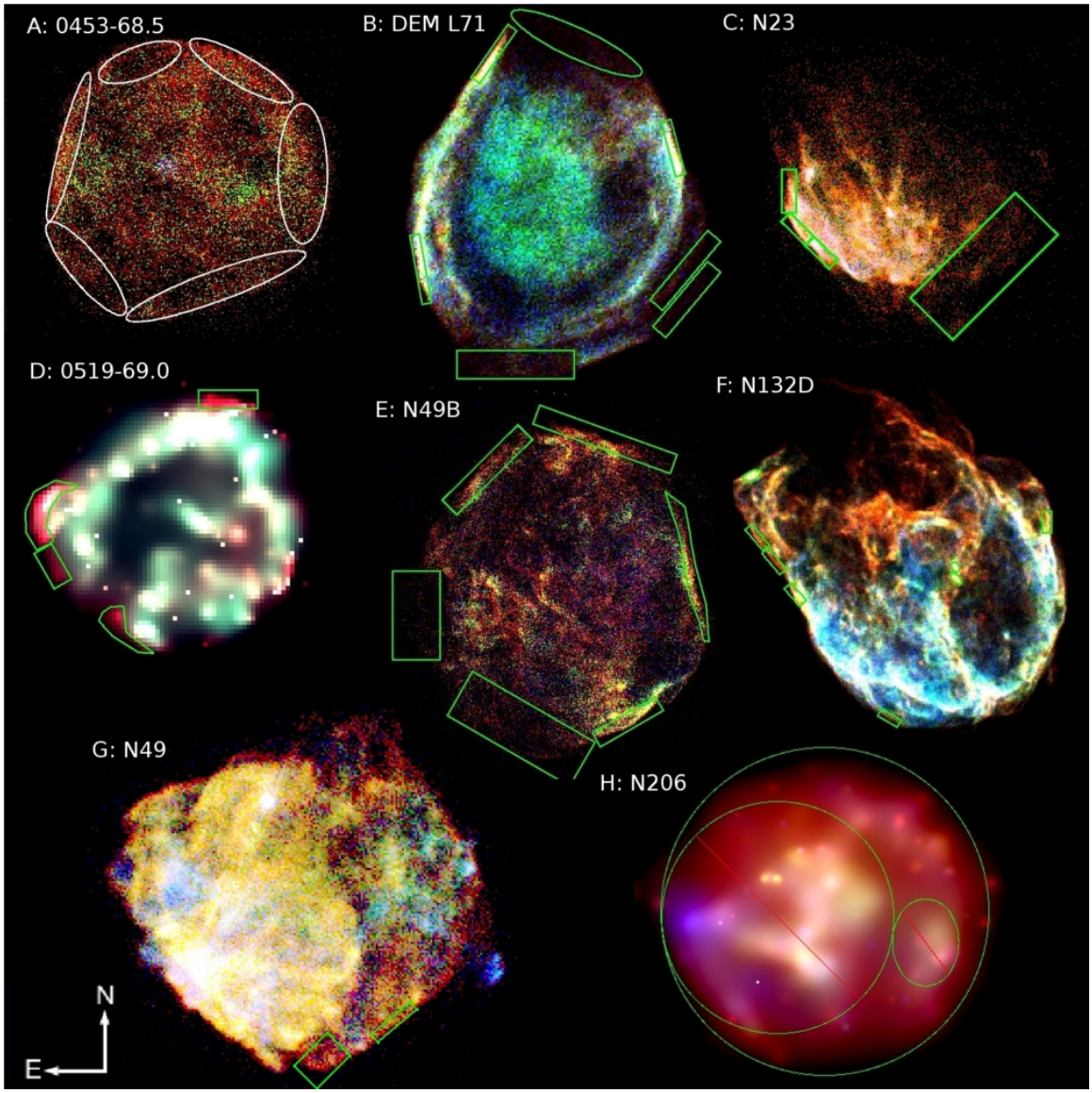

Figure 2.1 3-color maps for individual SNRs. ISM regions used for spectral modeling are overlaid. Color codes are red: 300–720 eV, green: 720–1100 eV, blue: 1100–7000 eV. 0519-69.0 and N206 have been adaptively smoothed to emphasize their faint ISM features.

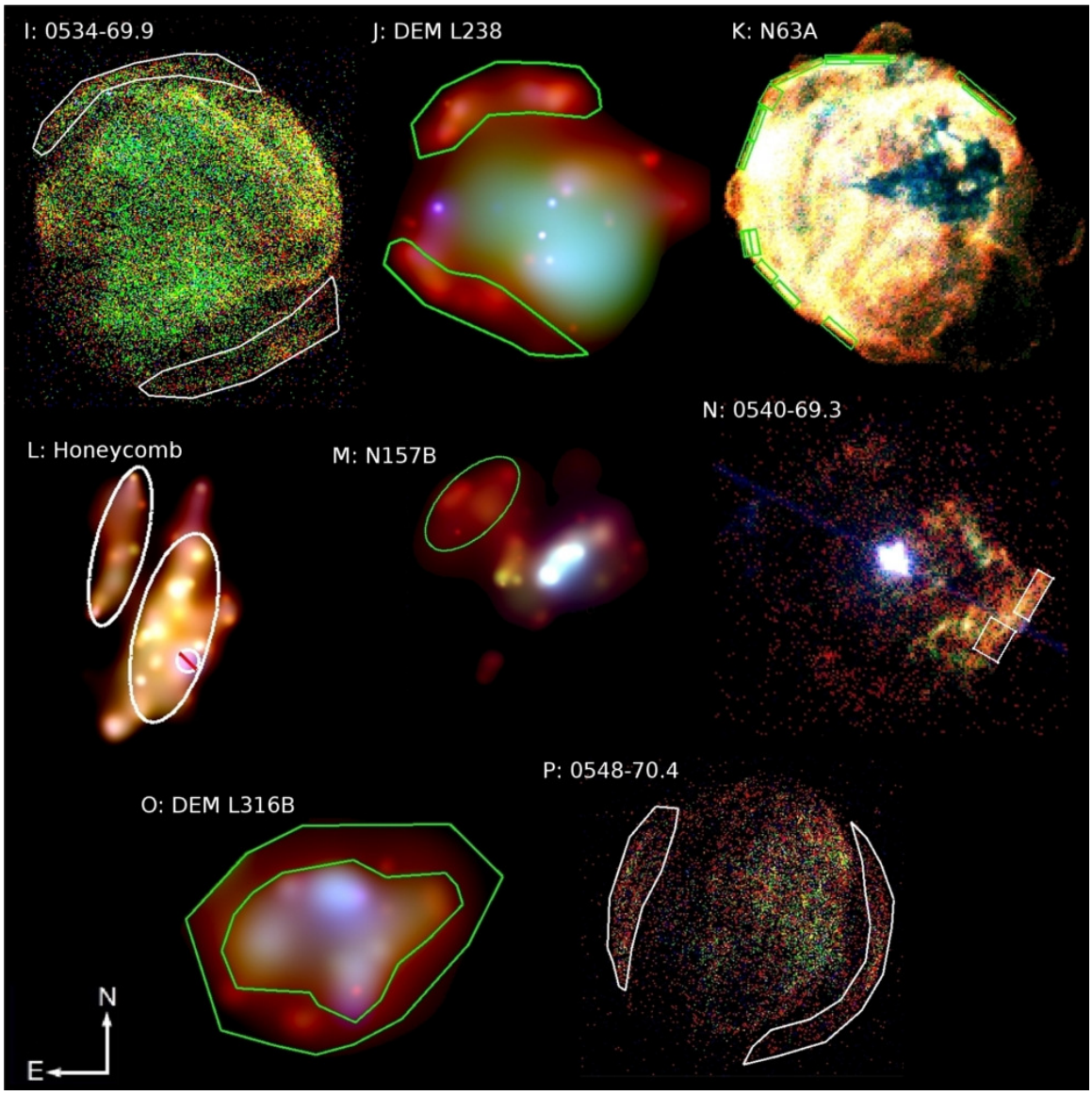

Figure 2.2 3-color maps for individual SNRs. ISM regions used for spectral modeling overlaid. Color codes are red: 300–720 eV, green: 720–1100 eV, blue: 1100–7000 eV. DEM L238, Honeycomb, N157B, and DEM L316B have been adaptively smoothed to emphasize their faint ISM features.

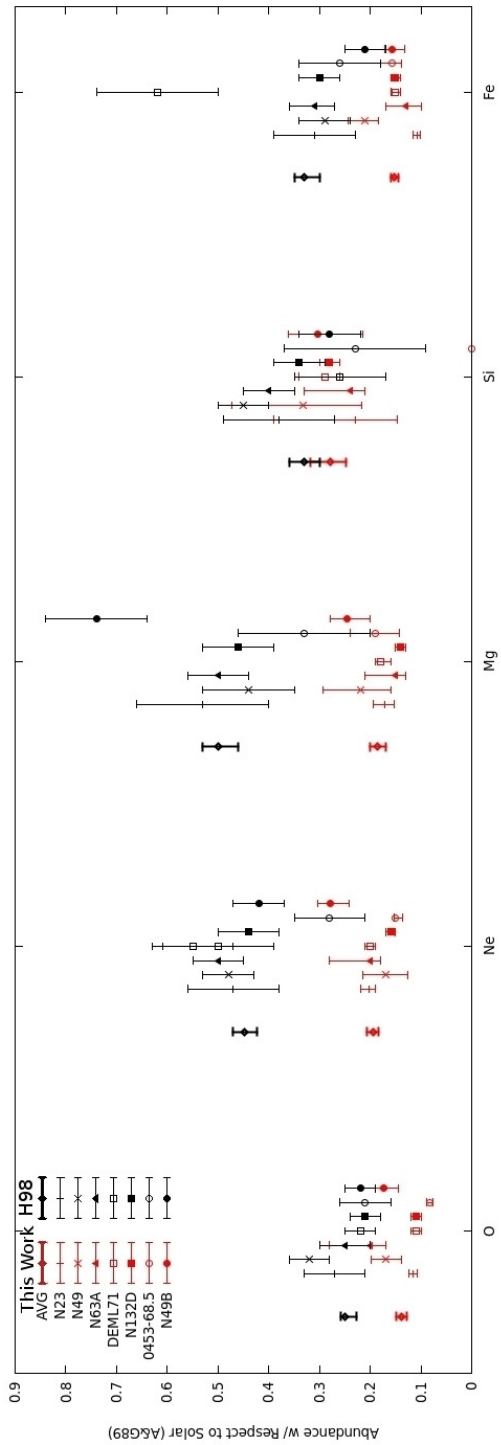

Figure 2.3 Abundance comparisons between H98 and this work for seven SNRs used in both works. The left-most data point for each element is the mean value for the seven SNRs.

Table 2.1. Archival *Chandra* Data of LMC SNRs

Target	ObsID(s)	RA(J2000)	Dec(J2000)	Total Exposure(ks)	Refs[c]
0453–68.5	1990	04 53 40	-68 29 45	38	1
DEM L71	3876 4440	05 05 42	-67 52 38	103	2
N23	2762	05 05 54	-68 01 37	37	3
0519–69.0	11241 12062 12063	05 19 35	-69 02 08	51	4
N49B	1041	05 25 25	-65 59 22	34	5
N132D	5532 7259 7266	05 25 03	-69 38 27	89	6
N49 [a]	10123 10806 10807 10808	05 26 01	-66 04 36	108	7
N206	3848 4421	05 32 00	-71 00 20	67	8
0534–69.9	1991	05 34 00	-69 55 00	59	9
DEM L238	3850	05 34 15	-70 33 42	67	10
N63A	777	05 35 44	-66 02 14	43	11
	1044 1967 2831				
Honeycomb [b]	2832 3829	05 35 45	-69 18 06	400	12
	3830 4614 4615				
N157B	2783	05 37 48	-69 10 20	48	13
0540–69.3	5549 7270 7271	05 40 11	-69 19 55	104	14
DEM L316B	2829	05 47 15	-69 42 25	35	15
0548–70.4	1992	05 47 50	-70 24 45	59	9

[a]There are two other ObsIDs (1041 and 2515) that detected N49 in the *Chandra* archive. Those observations are not useful because of a large off-axis pointing ($\sim 6\farcm5$ for ObsID 1041) and a short exposure ($\sim$7 ks for ObsID 2515). Thus we excluded them in this work.

[b]Honeycomb nebula has not been the target object in any *Chandra* observations. However, Honeycomb is in close proximity to SNR 1987A ($\sim 1.7'$ south) and is thus detected on several SNR 1987A observations. We used 8 ObsIDs of SNR 1987A that include Honeycomb.

[c]1. Gaensler et al. (2003); McEntaffer et al. (2012) 2. Hughes et al. (2003) 3. Hughes et al. (2006) 4. Hughes et al. (1995); Kosenko et al. (2010) 5. Park et al. (2003a) 6. Banas et al. (1997); Sano et al. (2015); Borkowski et al. (2007) 7. Park et al. (2003b); Park et al. (2012) 8. Williams et al. (2005) 9. Hendrick et al. (2003) 10. Borkowski et al. (2006a) 11. Warren et al. (2003) 12. Chu et al. (1995) 13. Chen et al. (2006) 14. Park et al. (2010) 15. Williams & Chu (2005)

Table 2.2. Results of LMC ISM Abundance Measurements

SNR Name	SNR Type	kT (keV)	$n_e t$ ($\times 10^{12} cm^{-3}$s)	O	Ne	Mg	Si	Fe	χ^2_ν[a]	SF[b]
N63A		$0.55^{+0.12}_{-0.02}$	$3.6^{+3.3}_{-2.1}$	$0.20^{+0.09}_{-0.03}$	$0.20^{+0.08}_{-0.02}$	$0.15^{+0.06}_{-0.02}$	$0.24^{+0.09}_{-0.03}$	$0.13^{+0.04}_{-0.02}$	1.1	y
N49		$0.70^{+0.04}_{-0.05}$	$2.1^{+3.5}_{-1.9}$	$0.17^{+0.03}_{-0.03}$	$0.17^{+0.05}_{-0.04}$	$0.22^{+0.07}_{-0.06}$	$0.33^{+0.14}_{-0.12}$	$0.21^{+0.03}_{-0.03}$	1.0	y
N49B		$0.52^{+0.02}_{-0.05}$	$2.1^{+3.1}_{-1.8}$	$0.17^{+0.02}_{-0.03}$	$0.28^{+0.03}_{-0.04}$	$0.25^{+0.03}_{-0.05}$	$0.30^{+0.06}_{-0.09}$	$0.16^{+0.01}_{-0.03}$	1.1	y
0453-68.5		$0.35^{+0.02}_{-0.03}$	$1.8^{+2.5}_{-2.3}$	$0.08^{+0.01}_{-0.01}$	$0.15^{+0.01}_{-0.01}$	$0.19^{+0.05}_{-0.05}$		$0.16^{+0.02}_{-0.02}$	1.2	n
0540-69.3	CC	$0.42^{+0.04}_{-0.05}$	$2.9^{+1.8}_{-2.0}$	$0.12^{+0.05}_{-0.03}$	$0.18^{+0.04}_{-0.03}$	$0.14^{+0.04}_{-0.01}$	$0.20^{+0.06}_{-0.05}$	$0.21^{+0.06}_{-0.04}$	1.1	y
N23		$0.47^{+0.02}_{-0.03}$	$0.4^{+1.2}_{-0.2}$	$0.12^{+0.01}_{-0.01}$	$0.20^{+0.02}_{-0.01}$	$0.17^{+0.02}_{-0.02}$	$0.23^{+0.16}_{-0.08}$	$0.11^{+0.01}_{-0.01}$	1.0	y
N157B		$0.60^{+0.25}_{-0.30}$	$0.6^{+2.0}_{-0.2}$	$0.09^{+0.17}_{-0.04}$	$0.24^{+0.27}_{-0.12}$	$0.12^{+0.18}_{-0.07}$		$0.05^{+0.08}_{-0.04}$	1.2	y
N206		$0.45^{+0.02}_{-0.01}$	$2.0^{+3.7}_{-1.5}$	$0.10^{+0.02}_{-0.01}$	$0.13^{+0.03}_{-0.03}$	$0.26^{+0.09}_{-0.07}$	$0.24^{+0.18}_{-0.14}$	$0.14^{+0.02}_{-0.02}$	1.1	y
DEM L316B		$0.49^{+0.10}_{-0.05}$	$25.0^{+5.0}_{-9.1}$	$0.17^{+0.51}_{-0.10}$	$0.20^{+0.23}_{-0.09}$	$0.20^{+0.12}_{-0.08}$	$0.25^{+0.20}_{-0.14}$	$0.08^{+0.11}_{-0.03}$	1.1	y
N132D		$0.73^{+0.02}_{-0.03}$	$1.2^{+1.5}_{-1.0}$	$0.11^{+0.01}_{-0.01}$	$0.16^{+0.01}_{-0.01}$	$0.14^{+0.01}_{-0.01}$	$0.28^{+0.02}_{-0.02}$	$0.15^{+0.01}_{-0.01}$	1.3	y
DEM L71		$0.45^{+0.01}_{-0.01}$	$2.7^{+3.4}_{-2.1}$	$0.11^{+0.01}_{-0.01}$	$0.20^{+0.01}_{-0.01}$	$0.18^{+0.01}_{-0.02}$	$0.29^{+0.05}_{-0.03}$	$0.15^{+0.01}_{-0.01}$	1.2	n
DEM L238		$0.44^{+0.04}_{-0.04}$	$0.7^{+1.5}_{-0.5}$	$0.06^{+0.01}_{-0.01}$	$0.11^{+0.05}_{-0.04}$	$0.15^{+0.14}_{-0.10}$		$0.12^{+0.05}_{-0.03}$	1.1	n
0519-69.0	Ia	$1.43^{+0.12}_{-0.15}$	$0.5^{+0.8}_{-0.4}$	$0.12^{+0.03}_{-0.02}$	$0.34^{+0.10}_{-0.09}$	$0.16^{+0.11}_{-0.08}$	$0.34^{+0.25}_{-0.20}$	$0.16^{+0.06}_{-0.04}$	1.2	n
0534-69.9		$0.33^{+0.02}_{-0.02}$	$3.2^{+5.5}_{-2.5}$	$0.10^{+0.01}_{-0.01}$	$0.21^{+0.03}_{-0.02}$	$0.21^{+0.07}_{-0.04}$	$0.42^{+0.25}_{-0.17}$	$0.20^{+0.03}_{-0.02}$	1.2	n
0548-70.4		$0.42^{+0.06}_{-0.04}$	$2.6^{+2.0}_{-1.5}$	$0.17^{+0.12}_{-0.05}$	$0.29^{+0.16}_{-0.08}$	$0.34^{+0.18}_{-0.14}$		$0.20^{+0.10}_{-0.05}$	1.2	n
Honeycomb	Unknown	$0.36^{+0.02}_{-0.01}$	$1.1^{+1.3}_{-0.8}$	$0.10^{+0.01}_{-0.02}$	$0.25^{+0.04}_{-0.03}$	$0.29^{+0.09}_{-0.08}$		$0.21^{+0.04}_{-0.03}$	1.1	y
Mean				$0.13^{+0.01}_{-0.01}$	$0.20^{+0.01}_{-0.01}$	$0.20^{+0.02}_{-0.01}$	$0.28^{+0.04}_{-0.03}$	$0.15^{+0.01}_{-0.01}$		
[X/H][c]				8.04 ± 0.04	7.39 ± 0.06	6.88 ± 0.06	6.99 ± 0.11	6.84 ± 0.05		
H98[d]				8.21 ± 0.07	7.55 ± 0.08	7.08 ± 0.07	7.04 ± 0.08	7.01 ± 0.11		

Note. — Abundances are relative to solar (Anders and Grevesse 1989). Statistical uncertainties are with 90% confidence errors. For some SNRs the Si abundance is fixed at Russell & Dopita (1992) value as we are unable to measure it due to poor photon statistics in the Si line feature.

[a]The average χ^2_ν of all spectral fits in the SNR.

[b]y: SNRs in a star-forming environment. n: SNRs in a non-star-forming environment.

[c]Mean abundances of this work expressed as [X/H] = 12 + Log(X/H), where X is the number density of an element and H is the number density of hydrogen.

[d]Mean abundances of H98 expressed as [X/H] = 12 + Log(X/H), where X is the number density of an element and H is the number density of hydrogen.

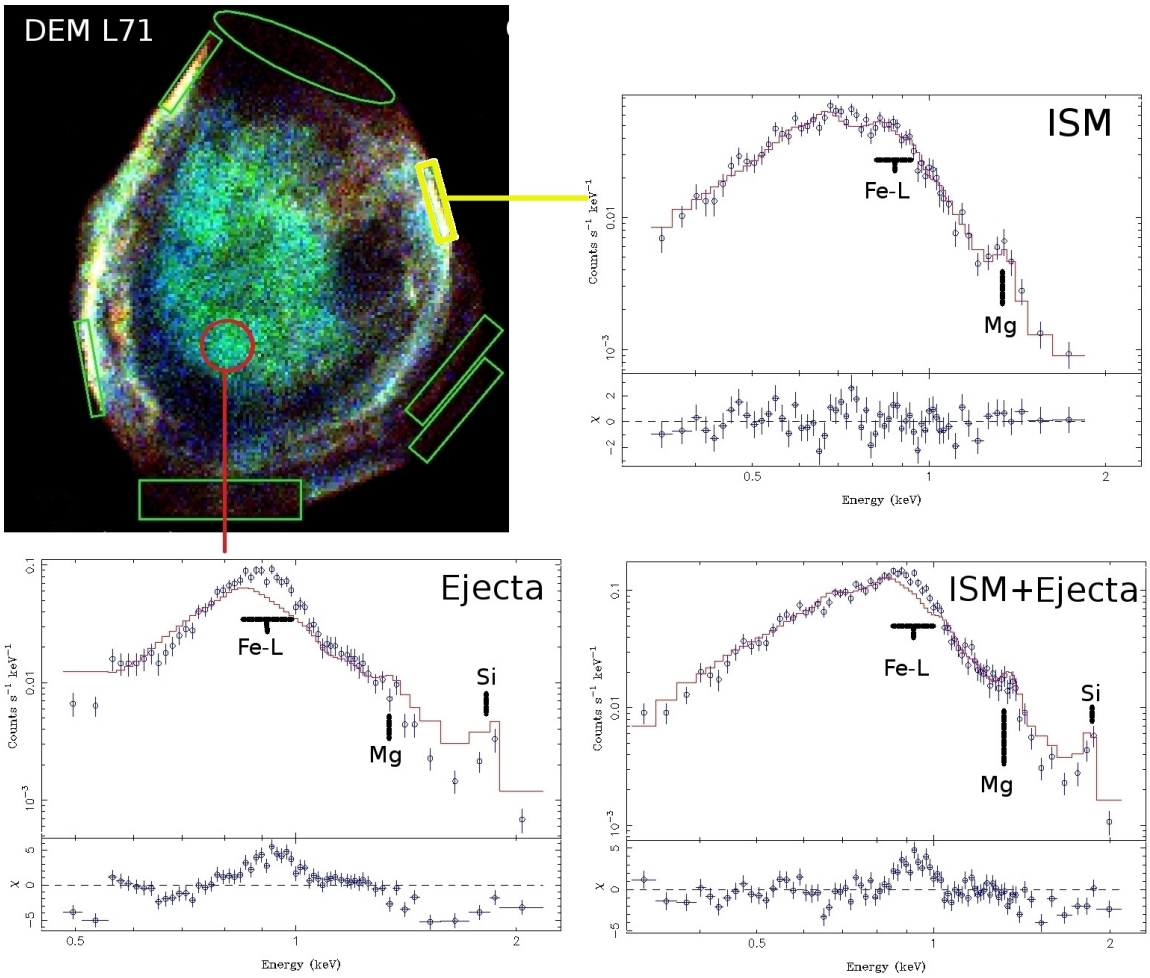

Figure 2.4 Spectral model fits for three representative regions in DEM L71. In all fits metal abundances are fixed at our measured LMC abundance values (Table 2.2). ISM-only (yellow region), metal-rich ejecta only (red region), and their combined spectra as shown. The residuals from the spectral model fits are shown at the bottom panel of each spectral plot. Green boxes are the other regions used in our ISM abundance measurements.

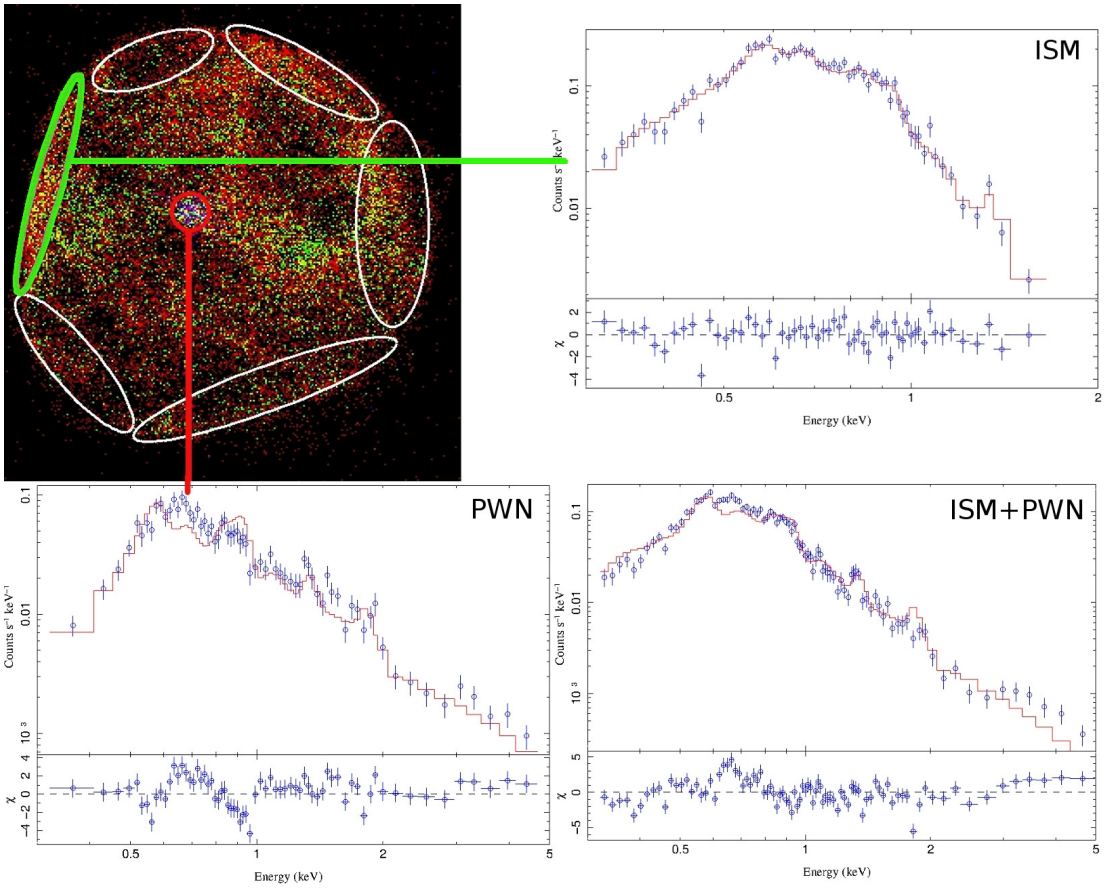

Figure 2.5 Spectral model fits for three representative regions in 0435-68.5. In all fits metal abundances are fixed at our measured LMC abundance values (Table 2.2). ISM-only (green region), PWN only (red region), and their combined spectra are shown. The residuals from the spectral model fits are shown at the bottom panel of each spectral plot. White ellipses show the other regions used in our ISM abundance measurements.

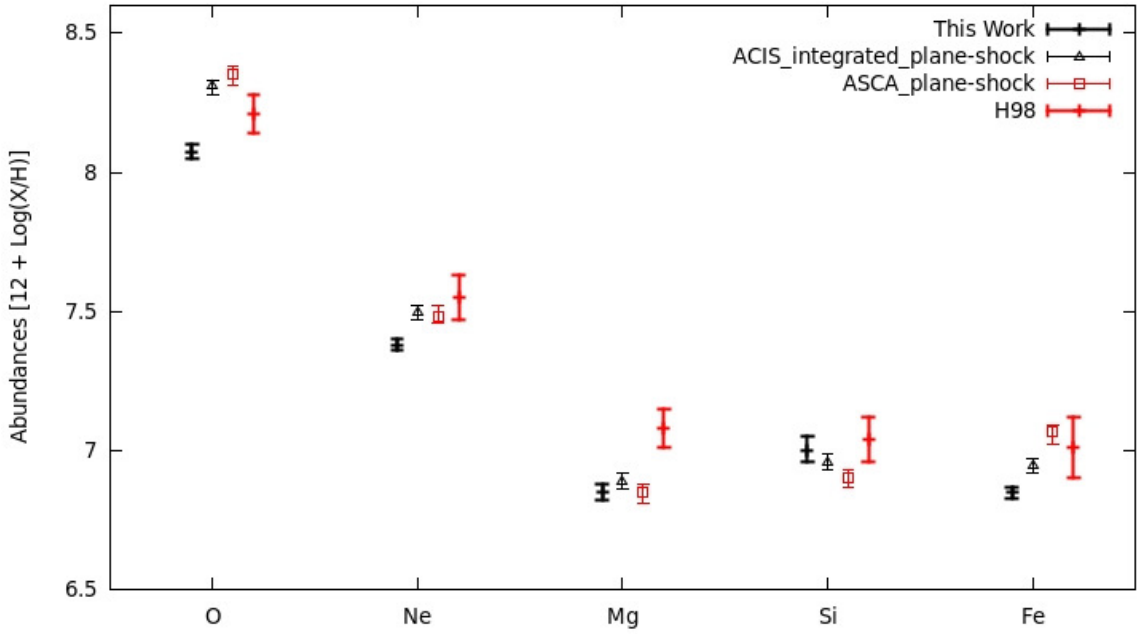

Figure 2.6 Averaged elemental abundances estimated by our plane-shock model fits to integrated ACIS and *ASCA* spectra of the seven SNRs used in H98. Elemental abundances from this work and H98 are also shown. Statistical uncertainties are with 90% confidence level.

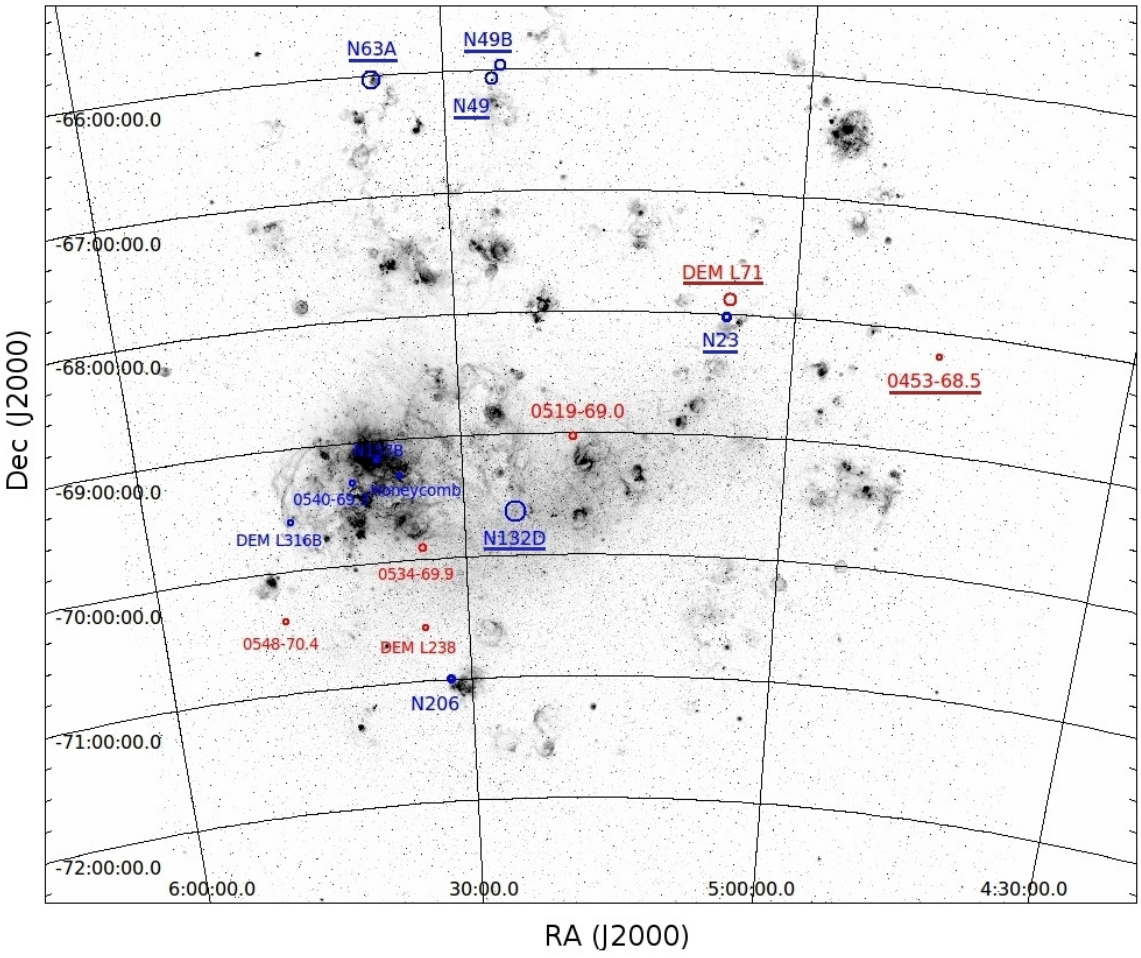

Figure 2.7 The Hα map of the LMC (Image Credit: C. Smith, S. Points, the Magellanic Cloud Emission-line Survey Team and National Optical Astronomy Observatory/Association of Universities for Research in Astronomy/National Science Foundation). Sixteen LMC SNRs used in this study are marked with circles. A larger circle implies a brighter SNR in a square-root scale. Blue circles indicate that the SNR is located within a star-formation region, while red circles indicate the SNR is located in a non-star-formation region. The SNRs used in H98 are underlined.

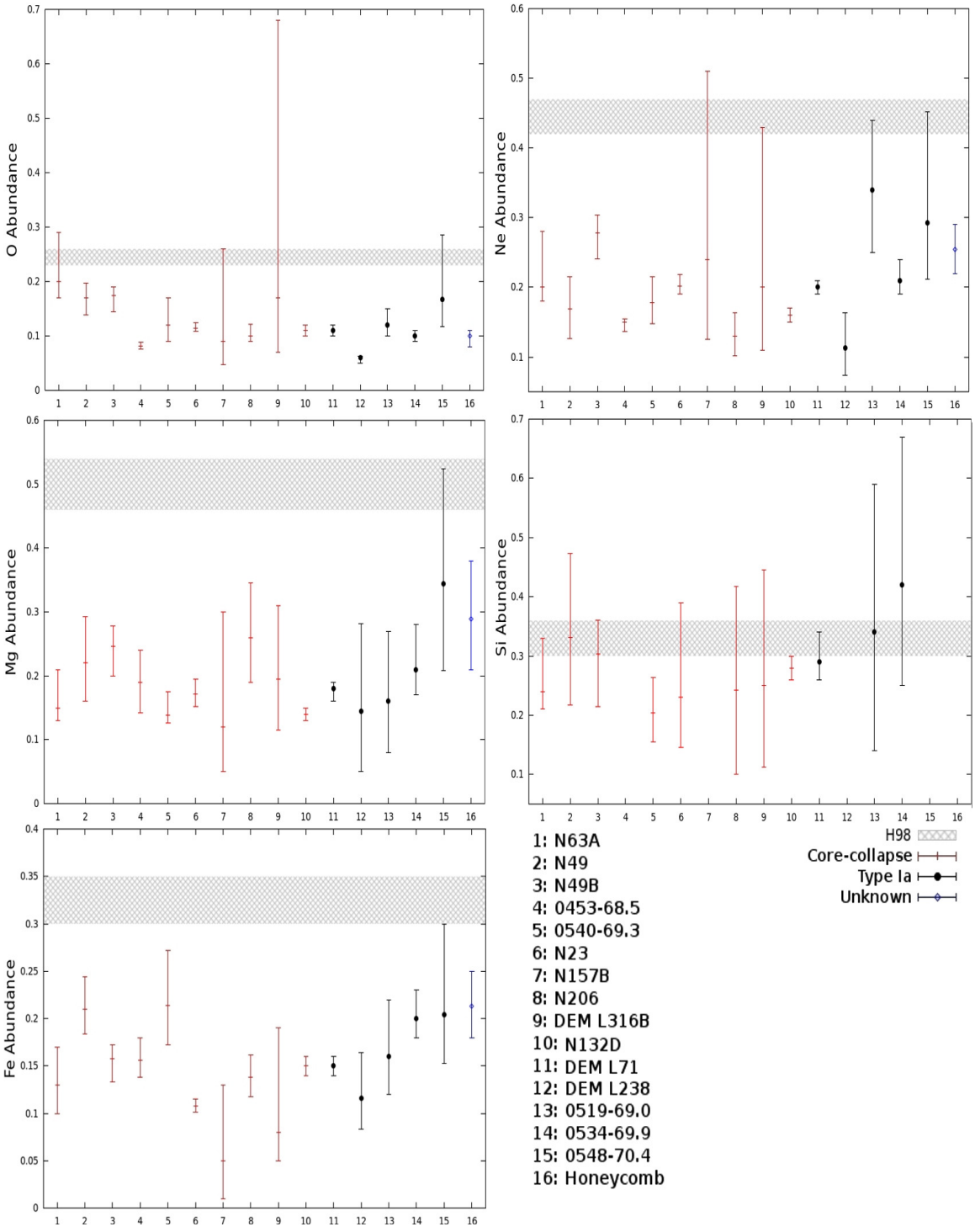

Figure 2.8 Elemental abundances for O, Ne, Mg, Si, and Fe for each SNR used in this study. Abundances are with respect to solar (Anders and Grevesse 1989).

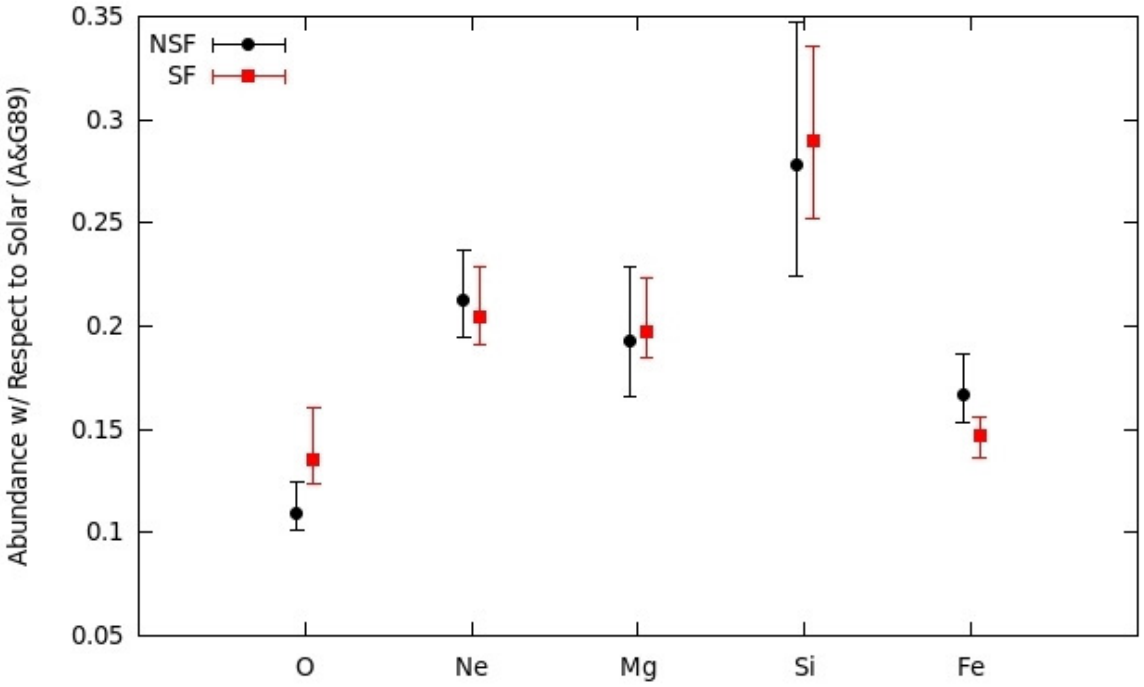

Figure 2.9 Comparisons between SNRs located within star formation (SF) regions and those found in regions without star formation (NSF).

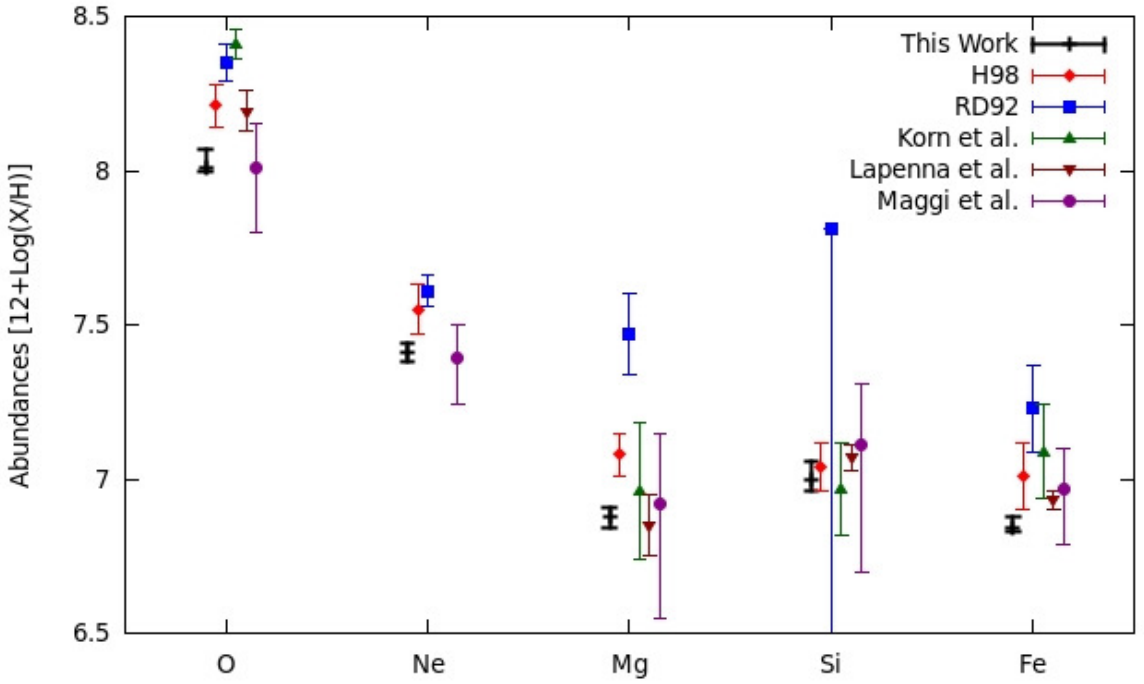

Figure 2.10 Abundance comparisons among this work and previous measurements.

CHAPTER 3

A Deep *Chandra* Observation of Oxygen-Rich Supernova Remnant B0049-73.6 in the Small Magellanic Cloud

3.1 INTRODUCTION

CC explosions of massive stars ($M \gtrsim 8M_{\odot}$) account for $\sim$3/4 of all SNe. These CC SNe directly affect the chemical evolution of the ISM surrounding them and, subsequently, the star-formation history of the host galaxy. X-ray observations of CC SNRs are useful to study some fundamental natures of CC SNe and their evolution such as the metal composition in the progenitor star, the explosive nucleosynthesis, and the chemical composition of the ISM into which the blast wave is expanding.

B0049-73.6 is a relatively old SNR (age $\sim$ 14,000 yr, Hendrick et al. 2005, H05 hereafter) in the SMC. Using the 50 ks *Chandra* observation H05 were able to resolve a bright central nebula surrounded by a faint outer shell. H05 found that the central nebula showed enhanced line emission from highly ionized H-like O and He- and H-like Ne ions. Atomic line emission from He-like Mg and Si ions also appeared enhanced. H05 concluded that the central nebula was metal-rich, particularly in O and Ne, which represents chemically-enriched stellar debris. Based on this ejecta composition H05 identified B0049-73.6 as the third member of the O-rich SNRs in the SMC (the other two being SNRs E0102-7219 [Dopita & Tuohy 1984] and 0103-72.6 [Park et al. 2003c]) and thus a CC SNR. The central ejecta nebula shows a distinct ring-like morphology (in projection) and is complicated in nature with apparent radial and azimuthal sub-structures. Assuming a common $\sim$15$M_{\odot}$ red supergiant progenitor for CC SNe H05 performed simple 1D hydrodynamic numerical simulations of SNRs to

study the observed dynamical structure (e.g., locations of the forward shock, reverse shock, and CD) of B0049-73.6. They found that a bright X-ray ejecta shell would form just interior to the CD that would have a radius of ∼10 pc at the age of B0049-73.6. The observed bright O-rich ring in B0049-73.6, which is presumed to represent the CD in this SNR, has a significantly smaller size (∼6 pc in radius) than that of the simulated CD. Thus H05 proposed an alternative scenario of an Fe-Ni bubble for the origin of the observed central ring-like nebula. However, its true origin remains elusive.

Here we report on the results from our deep ∼450 ks *Chandra* observation of B0049-73.6. Based on these new *Chandra* data, which are ∼8 times deeper than those used by H05, we reveal that the true extent of the central ejecta nebula is larger than the size of the bright O-rich ring, being consistent with the size of the CD estimated by H05's 1D hydrodynamical model. We detect several new emission features that suggest a highly asymmetrical distribution of metal-rich ejecta in B0049-73.6. We have published these results in *The Astrophysical Journal* (Schenck et al. 2014). Based on Schenck et al. (2014) we present our results in the following sections. In Section 3.2 we describe our observations and data reduction. In Section 3.3 we present the results from our imaging and spectral data analyses. A discussion and conclusions are presented in Section 3.4.

3.2 OBSERVATIONS & DATA REDUCTION

We performed our *Chandra* observations of B0049-73.6, which comprise 17 ObsIDs, between 2010 April 14 and 2010 June 2 (Table 3.1). We chose the ACIS-S3 with the SNR centered on the aim point to utilize the high sensitivity of the S3 chip in the soft X-ray band ($E \lesssim 1$ keV). Data were gathered in Very Faint mode and processed with CIAO version 4.5 via the *chandra_repro* script with CALDB version

4.5.5, which includes corrections for the charge transfer inefficiency and recent change of the contamination rate in the optical blocking filter, which affected the quantum efficiency of the ACIS by an additional ∼15% since mid-2009. Filtering was done for the standard ASCA grades (0,2,3,4,6) and for photon energies between 0.3 and 3.0 keV, beyond which the SNR emission is negligible. The overall light curve showed no significant flaring background. We performed this data reduction on each individual observation. After the data reduction the total effective exposure is ∼441 ks.

3.3 ANALYSIS & RESULTS

3.3.1 Imaging Analysis

In Figure 3.1 we show an X-ray three-color image of B0049-73.6, based on our deep *Chandra* data. The color codes are red: 300-700 eV, green: 700-1100 eV, and blue: 1100-3000 eV. The red and blue bands are on a square-root scale while the green band is on a log scale. We combined all individual observations of B0049-73.6 and ran the CIAO tool *wavdetect* on the combined data to detect point sources. Although all detected point sources are faint (the combined point source flux makes up ∼2% of the total SNR flux) we removed all of them before creating images and before performing any data analysis. We binned each color image by 2×2 pixels and then adaptively smoothed them. The small-scale (∼several arcseconds) clumpy features in Figure 3.1 are likely an artifact of the adaptive smoothing process. The main outermost boundary shows a nearly circular shell-like morphology and is spectrally soft (red). This outer shell was identified as the swept-up ISM by H05, and our spectral analysis confirms it (see Section 3.3.2). The radius of the outermost boundary is 1′.2 from the SNR center. We detect a faint emission feature in the northeast extending beyond the main outermost shell (the "Ear" in Figure 3.1b) which was not detected

in the previous data. In contrast to the outer shell, the central nebulosity shows various colors throughout, which indicate a significant contribution from higher energy photons, probably from line emission of various elemental species. This complex color structure of the central nebula is generally consistent with the metal-rich ejecta origin suggested by H05. The central ring-like nebulosity peaks in brightness at $\sim 20''$ from the SNR center. This intensity peak corresponds to the O-rich ring identified by H05. Based on our data with a deep exposure, we detect the diffuse emission defining the main outer boundary of this central ejecta nebula, which extends beyond the broadband intensity peak out to $\sim 40''$ from the SNR center. The central nebula shows asymmetric emission features including an elongated feature in the southern part and various areas of deformation primarily in the east. It is remarkable that a spectrally-hard (blue) emission feature in the western part of the central ejecta nebula extends out to the western outermost shell (Region A in Figure 3.1b).

Figure 3.2 shows *equivalent-width* images (EWI) for O-Lyα ($E \sim 0.65$ keV), Ne-Heα ($E \sim 0.90$ keV), Ne-Lyα ($E \sim 1.02$ keV), and Si-Heα ($E \sim 1.84$ keV) line emission. To create these EWI maps we followed the method found in literature (e.g.,Hwang et al. 2000; Park et al. 2002). We selected emission line bands: O-Lyα = 620–650, Ne-Heα = 850–950, Ne-Lyα = 1000–1100, and Si-Heα = 1700–1900 eV. Images in these bands were binned by 2×2 pixels and then adaptively smoothed prior to EW calculations. The underlying continuum was calculated by logarithmically interpolating the fluxes from the higher and lower continuum images of narrow energy bands nearby the line center energy. The estimated continuum flux was integrated over the line band and subtracted from the line emission flux. The continuum-subtracted line intensity was then divided by the estimated continuum flux on a pixel-by-pixel basis to generate the EWI for each line. In order to avoid noise in the EW maps caused by pixels with poor photon statistics, we set the EW

values to zero on pixels where the calculated continuum flux is $\lesssim 10\%$ of the total flux. Small scale variations in Figure 3.2 ($\lesssim$ several arcseconds which correspond to typical smoothing scales) are likely statistical artifacts. We note that we use these EWIs only for a qualitative guide to track line-enhanced/suppressed areas for an efficient regional spectral analysis. We do not attempt any quantitative interpretations directly from the EWIs. We extracted several characteristic regions based on our EWIs (Region A, Ear, and Regions 1 and 2 in Figure 3.1), and found that actual X-ray spectra from regions of our interest are consistent with the features implied by the EWIs (see Section 3.4).

O-Lyα EW is enhanced throughout the entire central ring-like nebulosity. While Ne-Heα EW distribution is generally similar to that of O-Lyα, several enhanced regions extend beyond the central ring toward the outermost boundary in the west (Region A in Figure 3.1b), northeast, and south. Ne-Heα EW is also enhanced in the Ear. Ne-Lyα enhancement is concentrated in the west (Region A) and in the Ear. Si-Heα EW is enhanced mainly in three distinct regions, two within the central nebulosity, and the other in Region A. Except for several small EW-enhanced features extending to the outer boundary, these EWIs are generally consistent with the previously-suggested metal-rich ejecta origin for the central ring-like nebulosity. On the other hand, the outer shell shows no enhancement in any EWI except for some small features discussed above (e.g. Region A). These low EWs in the outer shell are in general agreement with its previously-identified origin as the swept-up ISM.

3.3.2 Spectroscopic Analysis

We extracted the spectrum from the Shell region shown in Figure 3.1b. We extracted this spectrum from each individual observation and then combined them using the CIAO script *combine_spectra*. Some small parts of the outer shell show

various colors while most of the shell is nearly pure red (Figure 3.1a). These small regions were excluded from our study of the swept-up ISM. The entire Shell region contained ∼27,000 counts (∼17,200 counts from the southeastern region and ∼9,800 counts from the northwestern region). We binned the spectrum to contain a minimum of 20 counts per energy channel. We fit the Shell spectrum using an NEI plane-parallel shock model (Borkowski et al. 2001) with two foreground absorption column components, one for the Galactic ($N_{H,Gal}$) and the other for the SMC ($N_{H,SMC}$) columns. We used NEI version 2.0 (in xspec) associated with ATOMDB (Smith et al. 2001) which was augmented to include inner shell lines and updated Fe-L lines (see Badenes et al. 2006). We performed the background subtraction using the spectrum extracted from source-free regions outside of the SNR. We fixed $N_{H,Gal}$ at 4.5×10^{20} cm^{-2} for the direction toward B0049-73.6 (Dickey & Lockman 1990). We fixed abundances in $N_{H,SMC}$ at values by Russell & Dopita (1992). We varied electron temperature (kT), ionization timescale ($n_e t$), and normalization in the plane-shock model. We initially fixed all elemental abundances in the plane-shock model at the values found in Russell & Dopita (1992). The fit was statistically rejected ($\chi^2_\nu = 3.3$). Residuals from the best-fit model were significant around O and Ne line energies. We refit the data with O and Ne abundances varied. This fit improved but it was still statistically unacceptable ($\chi^2_\nu = 2.0$). We then varied each additional elemental abundance (for Mg, Si, and Fe) one at a time to improve the fit. We found that it was necessary to vary O, Ne, Mg, and Fe to obtain the statistically acceptable best-fit model ($\chi^2_\nu = 1.4$, Figure 3.3a). We note that varying the Si abundance did not make a statistically significant improvement in the fit based on an F-test (F-probability = 0.4). It is notable that the best-fit abundances for the fitted elements are significantly lower (by a factor of ∼3–4) than those by Russell & Dopita (1992). This low abundance is unlikely an artifact caused by underlying synchrotron emission

(from the relativistically accelerated electrons in the post-shock regions) because the observed X-ray spectrum is very soft and there is no observational evidence of thin filaments whose X-ray spectrum is dominated by a spectrally-hard continuum. Based on our inferred abundances we conclude that the Shell region is the swept-up ISM with very low metal abundances. Our best-fit model parameters for the Shell region are listed in Table 3.2.

The Region A's spectrum contains ∼8,000 counts, and shows distinct features compared to the swept-up ISM (Figure 3.3a). A broad line complex at E = 0.8–1.1 keV along with evident Mg(∼1.35 keV) and Si(∼1.85 keV) lines are present. This spectrum cannot be fit by a single shock model with abundances that we estimated for the Shell region ($\chi^2_\nu = 3.2$). These indicate the presence of an additional emission component superposed with the projected Shell emission. Thus, we used a two-component NEI shock model to fit this spectrum, one for the underlying Shell spectrum and the other responsible for the distinctive component in Region A. We fixed $N_{H,SMC}$ at the Shell value. We fixed all model parameters (except for normalization) of the underlying swept-up ISM component at the values for the Shell region. For the second shock component we initially allowed kT, $n_e t$, and normalization to vary and fixed the elemental abundances at the Shell values. The fit was not statistically acceptable ($\chi^2_\nu = 3.0$) because the model was not able to reproduce emission lines from various elements. We then thawed elemental abundances for the second component to improve the fit. The best-fit model required us to fit O, Ne, Mg, and Si ($\chi^2_\nu = 1.4$). The Ne and Si abundances are significantly enhanced compared to those of the Shell region: by ∼an order of magnitude for Ne and by a factor of ∼2 for Si. O and Mg overabundances are marginal (within 90% uncertainties of those for the Shell region). The best-fit model parameters for Region A are listed in Table 3.2.

We fit Regions 1 (∼12,500 counts) and 2 (∼16,800 counts) spectra (Figure 3.1b) using a one-component plane-shock model (Figure 3.3b). Initially we varied kT, $n_e t$, and normalization while fixing $N_{H,Gal}$, $N_{H,SMC}$, and all elemental abundances at the Shell values. The fit was statistically rejected for both regions ($\chi^2_\nu \gtrsim 4.0$). We then varied abundances for elements for which emission line features are associated with significant residuals from the best-fit model. We found that it was necessary to vary O, Ne, Mg, Si, and Fe abundances in Region 1 to obtain a satisfactory fit ($\chi^2_\nu = 1.4$). It was necessary to vary O, Ne, Mg and Si abundances for Region 2 ($\chi^2_\nu = 1.6$). The overall abundances for Regions 1 and 2 are significantly enhanced compared to the Shell abundances (by a factor of ∼3–6). Although our single-shock model fits for Regions 1 and 2 are statistically acceptable, they may have not adequately accounted for the superposed outer shell emission. To test this geometrical effect, we re-fit these spectra with a two-component shock model, adding a plane shock model component for the superposed outer shell spectrum. For the outer shell component we fixed all parameters at the Shell values except for normalization. The addition of the outer Shell component did not significantly affect the results because the contribution from the Shell is small (∼10–20% of the total flux). Thus we used our results from the one-shock model fits as summarized in Table 3.2 for the discussion of Regions 1 and 2 in the following sections.

The overall central ejecta nebula appears to extend beyond the intensity peak of the central ring (Figure 3.1a). To verify this extent of the central ejecta feature we investigate radial distributions of metal abundances based on spectra from 8 representative radial regions (dashed regions in Figure 3.1b.) We choose this azimuthal sector because it shows well-defined structures of both the central ejecta nebula and the outer shell along the radius of the SNR. The extracted spectrum from each of these eight radial sectors contains ∼2,500–4,500 counts. We initially fit each regional

spectrum with the one-component plane-shock model with all elemental abundances fixed at the Shell values. We allowed electron temperature, ionization timescale, and normalization to vary while fixing $N_{H,SMC}$ to the Shell value. This single shock model fit is acceptable in the outer regions at $r \gtrsim 40''$ ($\chi^2_\nu \lesssim 1.5$). For inner regions at $r \lesssim 40''$ the single shock model fits are not statistically acceptable ($\chi^2_\nu \gtrsim 2.0$, Figure 3.5b), probably because of a significant contribution from central ejecta emission. Thus, we used the two-component shock model for the inner regions at $r \lesssim 40''$, one for the ejecta component and the other for the superposed outer shell component. The parameters (except for normalization) for the underlying outer shell spectrum were fixed at the Shell values. Then we were able to obtain acceptable fits for all of the inner regions ($\chi^2_\nu \lesssim 1.4$). It was required to fit O and Ne abundances in the ejecta model component for these inner radial regions. The overall O and Ne abundances for the ejecta component in these inner regions are significantly enhanced compared to the Shell by a factor of $\sim$3–6, which are consistent with those for Regions 1 and 2. Our best-fit elemental abundances among individual inner ejecta regions are consistent within uncertainties. The best-fit model parameters for these radial regions are listed in Table 3.3.

3.3.3 Limits on the X-ray Luminosity of the Embedded Compact Remnant

Based on our deep *Chandra* data we place a tight upper limit on the X-ray luminosity of the embedded compact remnant that must have been created in this CC explosion. Using the MARX[1] software, we simulated point-like sources with a wide range of the 0.3–3 keV band luminosity. In these simulations we assumed a blackbody spectrum from the surface cooling of a neutron star (with a radius $r = 10$ km) and the foreground column appropriate for B0049-73.6. We simulated these point

[1] `http://space.mit.edu/ASC/MARX/`

sources with various temperatures and then added them to the center of the SNR's 0.3–3.0 keV band image to run the point source detection. We estimate a 3σ upper limit on the 0.3–7.0 keV band luminosity for the assumed point source to be $L_X \sim 6.0 \times 10^{32}$ erg s^{-1} corresponding to a blackbody temperature of $kT_{BB} \sim 0.09$ keV.

We compare our new luminosity (and thus surface temperature) upper limit with neutron star cooling models (Figure 3.4, Yakovlev & Pethick [2004]; Aguilera et al.[2008]) to constrain certain physical parameters of the embedded compact remnant, namely, mass and magnetic field. For comparisons, we add the previously-estimated temperature limit (Weisskopf & Hughes 2006) in Figure 3.4. Our estimated upper limit is consistent with the neutron star mass $M \gtrsim 1.1 M_{\odot}$, while the previous upper limit provided no constraint (Figure 3.4a). Our temperature limit is consistent with the magnetic field $B \lesssim 10^{13} G$, while the magnetic field is not well constrained by the previous upper limit (Figure 3.4b).

3.4 DISCUSSION

The central ejecta nebula is enriched in O, Ne, Mg, and Si. While O-, Ne-, and Mg-rich ejecta appear to show *smooth* distributions along the bright ring-like feature, our estimated Si abundances are significantly different between Regions 1 and 2. The overall metal abundances in Regions 1 and 2 are significantly higher than those of the Shell region, which indicates that these regions are the overabundant ejecta gas. Region A's spectrum indicates the presence of ejecta material that is enhanced in Ne and Si. It is remarkable that Region A extends from within the central ejecta nebula out to the outermost ISM shell. The Ear is a faint feature and clearly extends beyond the outer swept-up shell. Our results from a single plane-shock model fit of this feature suggest a significantly enhanced O and Ne abundances, compared to those in the Shell region, (although uncertainties are large due to low photon statistics), O

$= 0.48^{+0.72}_{-0.29}$ and Ne $= 0.96^{+0.79}_{-0.50}$ ($\chi^2_\nu = 26/24$). We show its observed spectrum and best-fit model in Figure 3.3a. The suggested Ne overabundance in the Ear region is consistent with the bright Ne line EWs shown in Figures 3.2b & 3.2c. Based on multi-wavelengths source catalogs through the HEASARC on-line database, we found a red giant projected within the boundary of the Ear. Considering the extended X-ray emission feature with likely-enhanced metal abundances for the Ear, this red giant is unlikely the counterpart for the Ear, and thus we conclude that the Ear is associated with the SNR. These results suggest that Regions A and Ear may be high-velocity ejecta material, similar to ejecta bullets found in other SNRs (e.g. Vela shrapnels [Aschenbach et al. 1995, Miyata et al. 2001], an ejecta bullet in N49 [Park et al. 2012]). These overall ejecta features show that the spatial distribution of metal-rich stellar debris in B0049-73.6 is far from spherically-symmetric. We note that, while the metal-rich ejecta shows an asymmetric distribution, the outermost forward shock boundary of B0049-73.6 is nearly circular. Such differential morphologies between the ejecta and swept-up shell have been observed in other relatively aged ($\gtrsim$ several 10^3 yr old) CC SNRs such as G292.0+1.8 (Park et al. 2007, Winkler et al. 2009) and Cygnus Loop (Katsuda et al. 2008).

Our radial spectral model fits show that overabundances for ejecta elements dominate the inner regions at $r \lesssim 40''$. These radial structures suggest that the central metal-rich ejecta nebula extends roughly out to $r \sim 40''$, corresponding to $\sim$10 pc from the SNR center at a distance of 60 kpc to the SMC (Hilditch et al. 2005, Pietrzynski, G., et al. 2013). We show the distributions of the broadband surface brightness and χ^2_ν from our one-component shock model fits along the radius of B0049-73.6 in Figures 3.4a & 3.4b. We also show the radial profile of the Ne abundance based on our best-fit spectral models (two-component model at $r \lesssim 10$ pc and one-shock at $r \gtrsim 10$ pc in Figure 3.5c). The O abundance shows a similar radial

profile to that of the Ne abundance. We show the fractional flux contribution from the ejecta-like emission component based on our two-component model fits for all radial regional spectra along the radius of B0049-73.6 (Figure 3.5d). We confirm that the contribution from the ejecta-like emission component in the total observed flux dominates for regions $r \lesssim 9$ pc and is significantly smaller for regions $r \gtrsim 9$ pc from the SNR center. It is evident that all of these parameters show significantly higher values at $r \lesssim 9$ pc than those at $r \gtrsim 9$ pc from the SNR center. These suggest the location of the CD at $r \sim 9$ pc, which extends significantly beyond the brightest part of the central ejecta nebula ($r \sim 5$ pc). This larger estimate for the CD is generally consistent with standard SNR dynamics as seen in one-dimensional hydrodynamical simulations by H05. A significant effect from the previously-suggested Fe-Ni bubble would not be required for our estimated size of the CD.

Based on the average values of the ejecta elemental abundances from Regions 1 and 2, we estimate the abundance ratios of O/Ne $= 3.0^{+1.1}_{-1.0}$, O/Mg $= 20.0^{+2.0}_{-1.4}$, and O/Si $= 4.0^{+3.3}_{-3.0}$. These ratios are in agreement with H05 except for O/Si which we measured to be $\sim$3 times lower. We note that H05 did not measure the O abundance of B0049-73.6 and only assumed a value 0.2 in their abundance ratio estimates. Also, our model fits use much better photon statistics and updated NEI modeling, and thus we consider our measurements more reliable than those by H05 (However, we note that our O/Si abundance estimate is based on two small regions where the Si abundance significantly varies. In this work we discuss the progenitor's nature based on these abundance ratios estimated from somewhat limited regions of the SNR. The abundance ratios measured from an extensive ejecta area, which is beyond the scope of this thesis, would be required to reach a more conclusive interpretation). These abundance ratios are in plausible agreement with the CC SN nucleosynthesis models for a 13–15$M_{\odot}$ progenitor with solar or sub-solar ($Z = 0.004$) metallicity (Nomoto et

al. 2006). It is notable that the Shell is significantly under-abundant compared to the general SMC values (Russell & Dopitca [1992]) by a factor of ∼3–4 for O, Ne, Mg, and Fe. This suggests that B0049-73.6 might have exploded in a locally metal-poor environment, which may support a low-Z progenitor.

Based on the volume EM (Equation 1.4) estimated from the spectral model fit of the Shell we calculate the post-shock electron density (n_e). For this estimate we assumed the X-ray emitting volume of $V \sim 3.0 \times 10^{58}$ cm^3 for our Shell region for a ∼3 pc path length (roughly corresponding to the angular thickness of the Shell region at 60 kpc) along the line of sight. We assumed $n_e \sim 1.2 n_H$ for a mean charge state with normal composition. Then our estimated electron density is $n_e \sim 2.4\ f^{-\frac{1}{2}}$ cm^{-3}, where f is the volume filling factor of the X-ray emitting gas. The pre-shock H density is $n_0 \sim 0.5\ f^{-\frac{1}{2}}$ cm^{-3} assuming a strong adiabatic shock where $n_H = 4\ n_0$. Based on their Sedov model fits H05 found that the post-shock regions of B0049-73.6 are in an electron-ion temperature equipartition. Ghavamian et al. (2007) found that several middle-aged SNRs have relatively low shock velocities and as such would be in electron-ion temperature equipartition. We thus assume electron-ion temperature equipartition for B0049-73.6 and then the gas temperature is related with the shock velocity (v_s) as $T = 3\hat{m}v_s^2/16k$ (where $\hat{m} \sim 0.6 m_p$ and m_p is the proton mass). For gas temperature of kT= 0.26 keV for the outer swept-up shell, we calculate a shock velocity of $v_s \sim 460$ km s^{-1}. Applying the Sedov solutions (Equations 1.1, 1.2, and 1.3) for the SNR with a radius of ∼20.5 pc, we estimate the dynamical age of $\tau_{sed} \sim 17,200$ yr for B0049-73.6 (in the case that the electron-ion temperature equipartition has not been established yet in B0049-73.6, our calculated v_s would be considered a lower limit, and therefor our SNR age estimate would be an upper limit.) We calculate the corresponding explosion energy of $E_0 \sim 1.7 \times 10^{51}$ erg (Equation 1.3). The total swept-up mass, $M_{SW} = n_0 m_p V$, is estimated to be $M_{SW} \sim 440\ f^{\frac{1}{2}}\ M_\odot$. Our

estimated Sedov age for B0049-73.6 is consistent with that of H05 within ∼20%. Our estimated E_0 is somewhat larger than the previous estimate (H05), but is consistent with the canonical value for a SN within a factor of ∼2. These results suggest that B0049-73.6 was probably created by a CC SN explosion (with a normal E_0) of a 13–15$M_\odot$ progenitor with a low metallicity.

Our estimated upper limit on the X-ray luminosity of the embedded compact stellar remnant at the center of B0049-73.6 is 2 orders of magnitude lower than the previous estimate ($L \sim 1.5 \times 10^{34}$ erg s^{-1} [Weisskopf & Hughes 2006]). Our tight estimate for the X-ray luminosity upper limit suggests that the compact stellar remnant of this SNR may belong to a peculiar class of low-luminosity neutron stars (e.g., the so-called Dim Isolated neutron stars, Mereghetti 2011) or may possibly be a black hole.

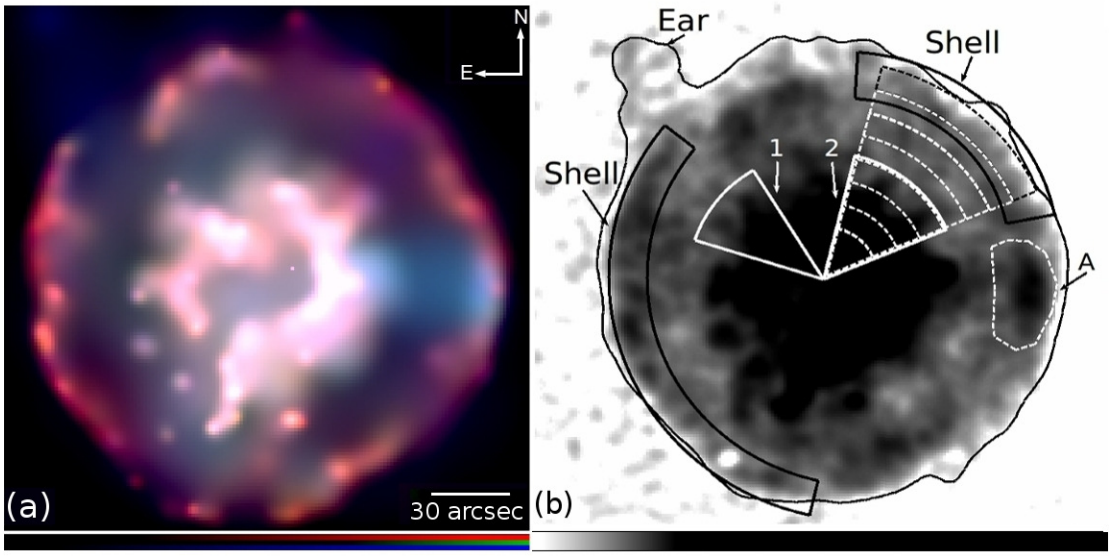

Figure 3.1 (a) A three-color image of B0049-73.6. Color codes are red: 300–700 eV, green: 700–1100 eV, and blue: 1100–3000 eV. Each color image has been binned by 2×2 pixels and then adaptively smoothed. The red and blue bands are on a square-root scale while the green band is on a log scale. (b) A grey-scale broadband image of B0049-73.6. The radial width of the dashed regions is ∼2.3 pc (8″) except for the innermost region for which it is ∼4.6 pc (16″). The central ring is saturated in black to emphasize faint outer regions. The overlaid contour marks the outermost boundary of B0049-73.6 based on the broadband image.

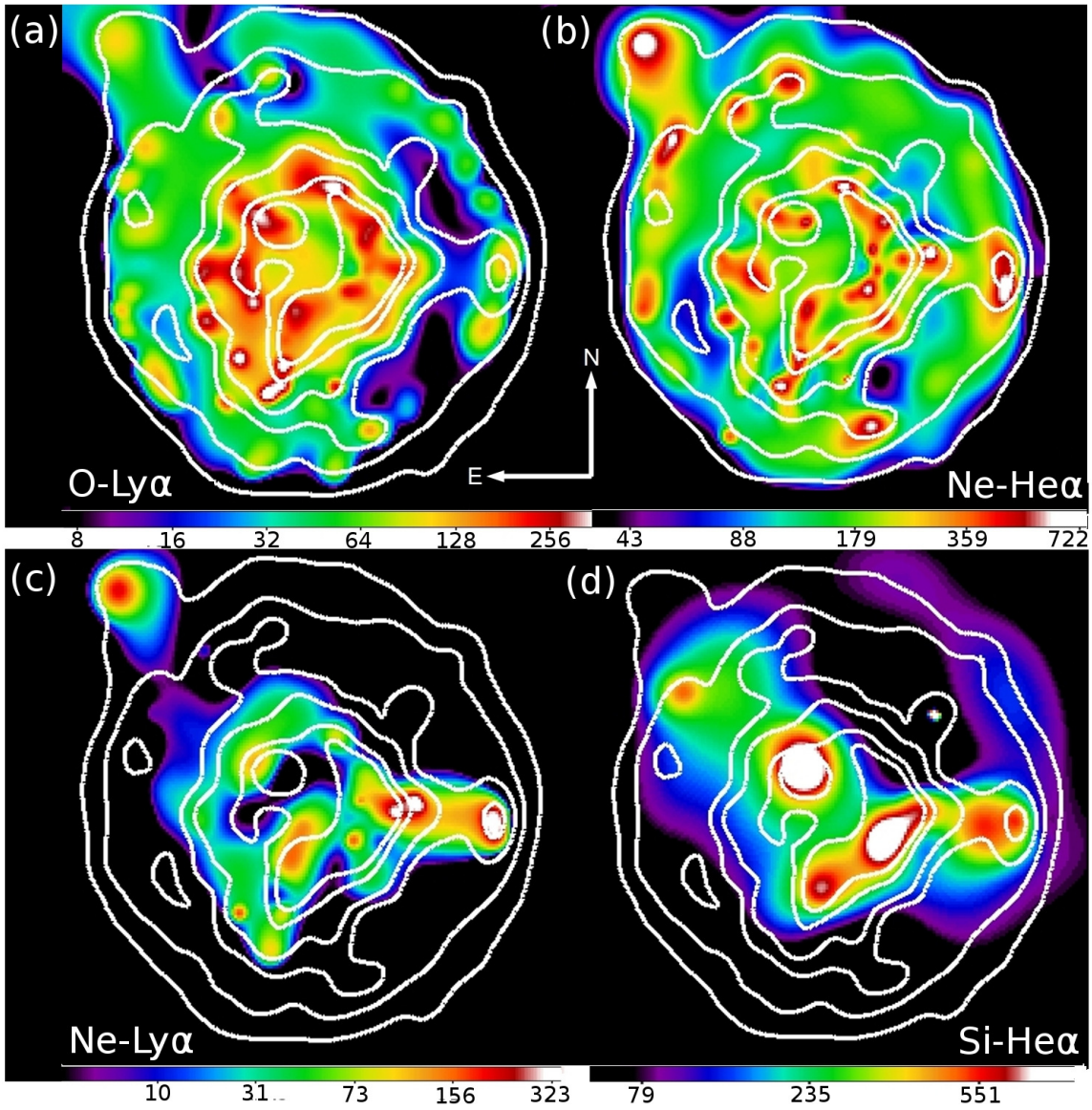

Figure 3.2 Line equivalent-width images of various elemental species for B0049-73.6. The false-color scales are in units of eV. Broadband image contours of the SNR are overlaid.

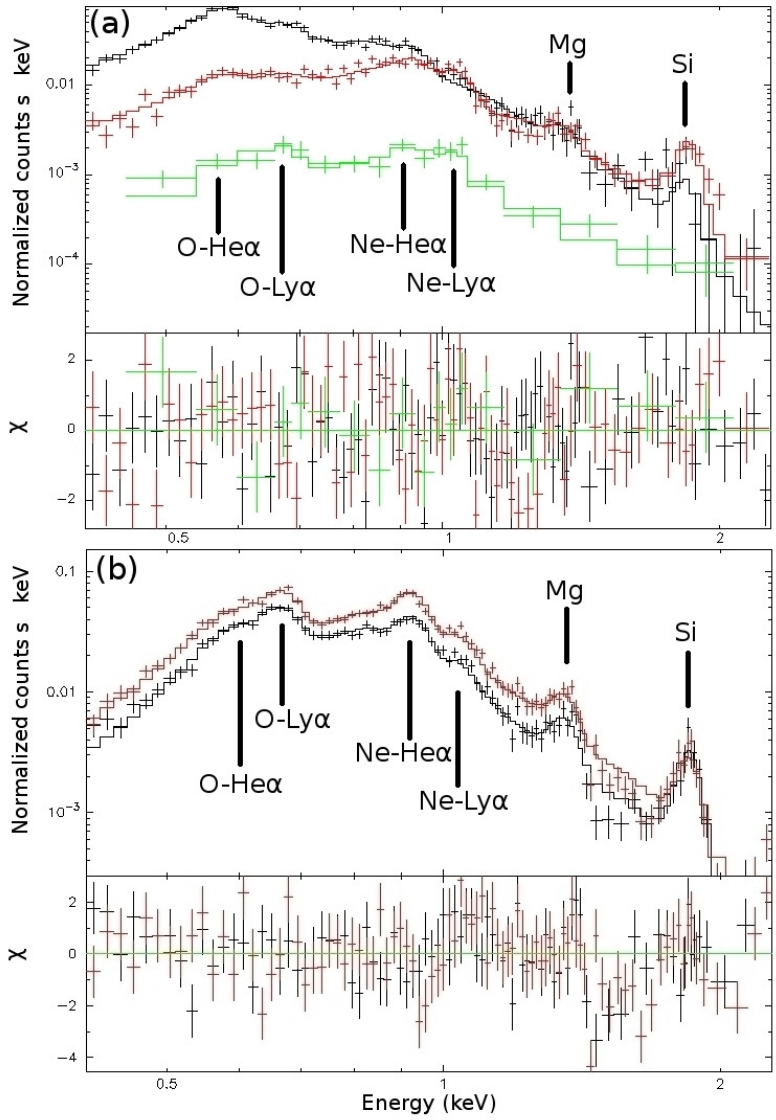

Figure 3.3 Observed spectra from selected regions within B0049-73.6 with the best-fit models overlaid. Residuals from these best-fit models are shown in the bottom panel. Several atomic emission line features are marked. (a) The ISM region is in black, Region A is in red, and the Ear region is in green. (b) Region 1 is in black and Region 2 is in red.

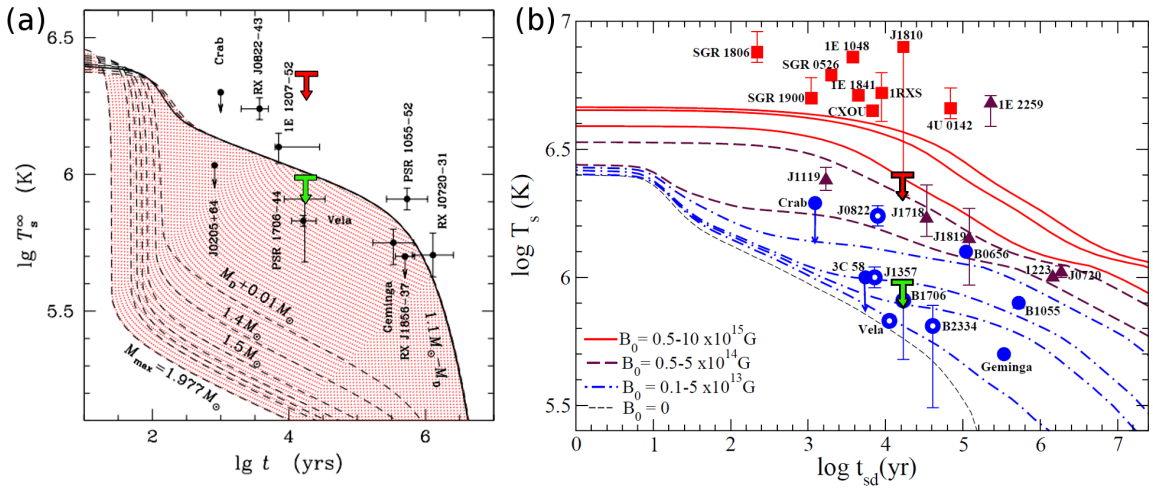

Figure 3.4 (a) Neutron star cooling curves with corresponding neutron star masses (Yakovlev & Pethick [2004]). (b) Neutron star cooling curves for several assumed magnetic fields (Aguilera et al.[2008]). The green downward arrow is the surface temperature upper limit from this work. The red downward arrow is the previous surface temperature upper limit from Weisskopf & Hughes (2006).

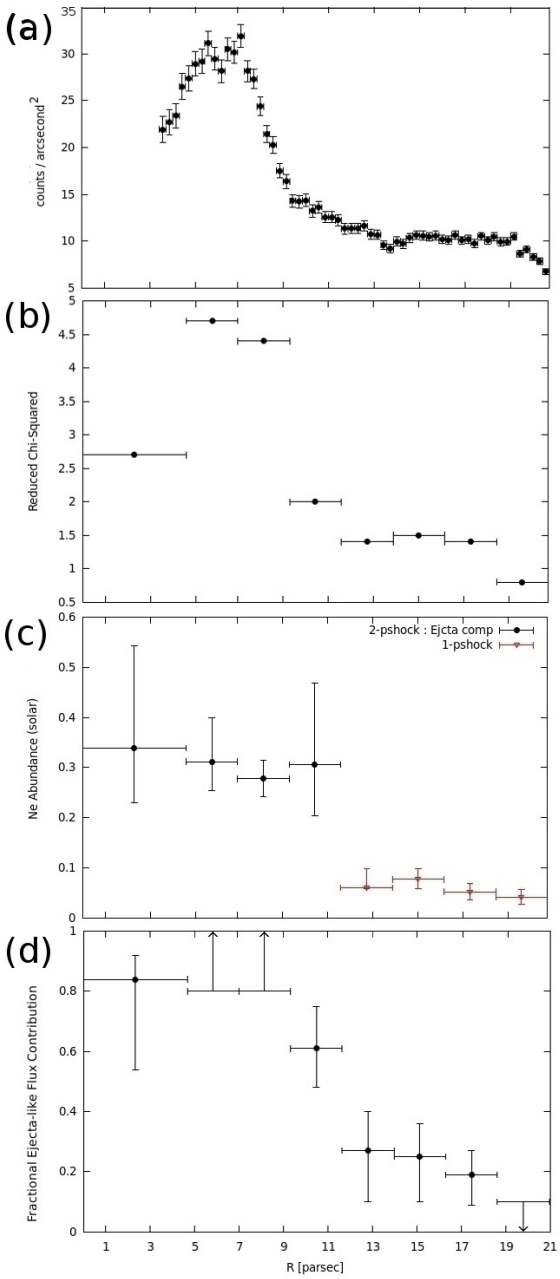

Figure 3.5 (a) A radial profile of the broadband surface brightness for B0049-73.6. Each radial bin size is ∼0.3 pc (1″). This radial profile is in the same direction as Region 2 (Figure 3.1b). 1σ uncertainties are shown. (b) χ^2_ν values from our one-component shock model fits with fixed Shell abundances along the radius of B0049-73.6. (c) The best-fit Ne abundance values along the radius of B0049-73.6. For $r \lesssim 10$ pc, they were based on the two-shock model fits (see text). (d) The fractional ejecta-component flux contribution based on our two-component model fits along the radius of B0049-73.6. Uncertainties for (c) and (d) are with a 90% confidence level.

Table 3.1. Our *Chandra* Observation Log of B0049-74.6

ObsID	Date	Exposure(ks)
11095	2010-05-18	18.80
11096	2010-06-02	36.57
11097	2010-04-14	29.60
11980	2010-04-21	22.75
11981	2010-05-01	33.60
11982	2010-05-03	24.57
11983	2010-05-12	29.34
11984	2010-05-22	20.48
11985	2010-05-25	20.77
12200	2010-04-22	26.73
12208	2010-05-02	15.97
12210	2010-05-07	27.55
12211	2010-05-04	34.99
12212	2010-05-14	18.31
12215	2010-05-19	22.75
12216	2010-05-22	28.67
12217	2010-05-28	28.67

Note. — The total combined exposure after the data reduction is $\sim$441 ks.

Table 3.2. Summary of Spectral Model Fits to Subregions of SNR B0049-73.6

Region	$N_{\rm H,SMC}$ (10^{21} cm^{-2})	kT (keV)	$n_e t$ (10^{12} cm^{-3} s)	EM (10^{57} cm^{-3})	χ^2/ν	O	Ne	Mg	Si	Fe
Shell	$0.15^{+0.04}_{-0.05}$	$0.26^{+0.04}_{-0.02}$	$0.25^{+0.06}_{-0.06}$	$80.50^{+30.90}_{-40.20}$	136/99	$0.03^{+0.01}_{-0.01}$	$0.04^{+0.01}_{-0.01}$	$0.06^{+0.04}_{-0.03}$	0.30[a]	$0.04^{+0.01}_{-0.01}$
A[b]	0.15[c]	$0.40^{+0.04}_{-0.03}$	> 5.00	$6.10^{+0.70}_{-1.40}$	125/88	$0.07^{+0.03}_{-0.04}$	$0.40^{+0.05}_{-0.08}$	$0.14^{+0.05}_{-0.06}$	$0.77^{+0.30}_{-0.25}$	0.04[d]
1	0.15[c]	$0.32^{+0.03}_{-0.03}$	$1.50^{+2.20}_{-0.48}$	$30.10^{+3.00}_{-5.00}$	137/93	$0.18^{+0.03}_{-0.03}$	$0.34^{+0.05}_{-0.05}$	$0.24^{+0.07}_{-0.07}$	$1.16^{+0.37}_{-0.31}$	$0.10^{+0.01}_{-0.03}$
2	0.15[c]	$0.34^{+0.01}_{-0.03}$	$1.10^{+1.30}_{-0.18}$	$28.00^{+8.20}_{-2.50}$	158/92	$0.12^{+0.01}_{-0.01}$	$0.24^{+0.02}_{-0.03}$	$0.15^{+0.02}_{-0.03}$	$0.37^{+0.10}_{-0.07}$	0.04[d]

Note. — Abundances are with respect to solar (Anders & Grevesse 1989). Uncertainties are with a 90% confidence level. The Galactic column $N_{\rm H,Gal}$ is fixed at 0.45×10^{21} cm^{-2}. For comparisons the Russell & Dopita (1992) values for SMC abundances are O = 0.126, Ne = 0.151, Mg = 0.251, Si = 0.302, Fe = 0.149.

[a]Si abundance was fixed at Russell & Dopita (1992) value for the SMC.

[b]The best-fit parameters of the ejecta component.

[c]$N_{H,SMC}$ was fixed at best-fit Shell value.

[d]Fe abundance was fixed at the best-fit Shell value.

Table 3.3. Summary of Spectral Model Fits to Radial Regions of SNR B0049-73.

Distance from center ($''$)	Counts	kT (keV)	$n_e t$ (10^{12} cm^{-3} s)	EM (10^{57} cm^{-3})	χ^2/ν	O	Ne
8[a]	2400	$0.35^{+0.09}_{-0.03}$	> 1.00	$3.10^{+1.40}_{-1.30}$	59/48	$0.15^{+0.10}_{-0.05}$	$0.31^{+0.15}_{-0.09}$
20[a]	4100	$0.35^{+0.05}_{-0.04}$	$1.10^{+1.00}_{-0.46}$	$5.80^{+1.70}_{-1.70}$	76/56	$0.14^{+0.04}_{-0.04}$	$0.30^{+0.07}_{-0.06}$
28[a]	4400	$0.31^{+0.04}_{-0.03}$	> 1.12	$10.50^{+1.90}_{-2.00}$	77/67	$0.15^{+0.04}_{-0.03}$	$0.26^{+0.05}_{-0.04}$
36[a]	3200	$0.33^{+0.10}_{-0.03}$	> 0.80	$3.60^{+1.60}_{-1.70}$	53/55	$0.17^{+0.10}_{-0.09}$	$0.30^{+0.14}_{-0.10}$
44	3100	$0.40^{+0.08}_{-0.06}$	$0.04^{+0.02}_{-0.01}$	$9.80^{+3.70}_{-3.40}$	78/56	$0.03^{+0.01}_{-0.01}$	$0.04^{+0.01}_{-0.02}$
52	3600	$0.36^{+0.06}_{-0.03}$	$0.05^{+0.03}_{-0.02}$	$3.80^{+1.00}_{-1.10}$	71/48	$0.03^{+0.01}_{-0.01}$	$0.07^{+0.02}_{-0.01}$
60	3900	$0.30^{+0.04}_{-0.02}$	$0.15^{+0.10}_{-0.05}$	$7.30^{+2.30}_{-2.60}$	80/55	$0.03^{+0.01}_{-0.01}$	$0.05^{+0.02}_{-0.01}$
68	3900	$0.24^{+0.03}_{-0.02}$	$0.18^{+0.13}_{-0.07}$	$14.50^{+4.80}_{-6.10}$	48/53	$0.03^{+0.01}_{-0.01}$	$0.04^{+0.01}_{-0.01}$

Note. — Abundances are with respect to solar (Anders & Grevesse 1989). Uncertainties are with a 90% confidence level. The Galactic column $N_{\rm H,Gal}$ is fixed at 0.45×10^{21} cm^{-2} and the SMC column $N_{\rm H,SMC}$ is fixed at the Shell value 0.15×10^{22} cm^{-2}. The Si abundance was fixed at the Russell & Dopitca (1992) value. The Mg and Fe abundance were fixed at the best-fit Shell value. The distance is from the SNR center to the center of each region corresponding to Figure 3.5.

[a]For these regions the best-fit parameters of the ejecta component are presented.

CHAPTER 4

Adaptive Mesh Analysis: Method and Application

4.1 Spatially-Resolved Spectroscopy of SNRs Using Adaptive Mesh Grid

Before the launch of *Chandra*, X-ray study of SNRs was limited to low-resolution imaging spectroscopy. In many cases only the integrated spectrum from the entire SNR was usable for spectral modeling. From this, astronomers were only able to paint general and/or basic pictures of SNRs and their properties. Thanks to *Chandra's* high resolution imaging spectroscopy, we are now able to resolve detailed sub-structures (with their spectral information) within the SNR. The high resolution data allow us to separate several distinctive emission components within a SNR such as shocked CSM/ISM, shock-accelerated synchrotron emission, PWN, and metal-rich ejecta. By analyzing these individual components we can reveal their spatial distribution of chemical composition, density, and thermal condition, all of which are critically important to reveal the nature of the progenitor system, explosion physics, and the shock interaction with the environment. For example, we may map the detailed spatial distributions of ejecta elements, and adequately estimate the total mass ejected by a SN. Such a detailed spatially-resolved spectral analysis may also help reveal interesting features of SNRs (e.g., the Mg rich region in N49B, Park et al. 2003a, or the "ejecta bullet" in N49, Park et al. 2010, to name only a few).

However, properly defining a number of small, characteristic sub-regions and analyzing spectra extracted from all of those numerous individual regions by hands are often unrealistically time-consuming, especially for deep observational data with rich photon statistics. Instead, it would be desirable to have an automated, adaptive,

sub-regional selection, and spectral model fits for the individual regional spectra. We developed our own software tool to apply an adaptive mesh grid over the entire surface of the SNR to automatically slice it into many small sub-regions with similar photon statistics and perform a spectroscopic analysis on each sub-region. In the following section we demonstrate the technique and utility of this method based on our example analysis of the archival *Chandra* ACIS data of SNR N63A in the LMC.

4.2 Application of Our Adaptive Mesh: Case of N63A

SNR N63A is a relatively young (∼2,000–5,000 yr old, Hughes et al. 2006) and bright SNR in the LMC. It contains many filamentary and knotty emission features throughout its interior, as well as "loops" and "plumes" near its outermost boundary (see Figure 2.2k). N63A is suggested to be dominated by emission from swept-up ISM, however, an in-depth exhaustive search for metal-rich ejecta in N63A has not been performed (Warren et al. 2003). Warren et al. (2003) noted that a thorough search would be necessary to determine if there are any regions of metal-rich ejecta. The archival *Chandra* data of N63A contain rich photon statistics (∼1 million photon counts). Thus, we chose N63A to demonstrate utility of our adaptive mesh grid method in an effort to search for the putative metal-rich ejecta features in this SNR.

We divided N63A into many small sub-regions utilizing our adaptive mesh grid. Each region in the grid was created by our automated software and constrained to contain a minimum of 3,000 photon counts in the 0.3-7 keV band. Our adaptive mesh created 346 regions for N63A (Figure 4.1). We decided not to include the southernmost "loops and plumes" in this study since they were very faint and are not suitable candidates for our adaptive mesh grid. We then extracted the spectrum from each region using our software. Finally, we performed spectral model fits for each regional spectrum utilizing an NEI plane-shock model with elemental abundances

fixed at our mean LMC ISM values (Table 2.2). We allowed the foreground absorption column, electron temperature, ionization timescale, and normalization to vary. This entire procedure (the adaptive grids, spectral extraction, and spectral model fits) is fully automated using our software. From these fits we created maps of the best-fit χ^2_ν for all 346 regions (Figure 4.2). We note that some sub-regions of N63A show a high χ^2_ν when their spectra are fitted with our new LMC abundances (particularly around the central parts of the SNR, Figure 4.2a). For these regions our LMC abundances underpredict the observed emission line fluxes, suggesting the presence of overabundant ejecta-dominated regions there. It is remarkable to reveal for the first time these candidate ejecta dominated regions in N63A. A detailed follow-up analysis of N63A is necessary, which is beyond the scope of this thesis.

These results from our preliminary study of N63A show the utility of our adaptive mesh grid method. We were able to efficiently perform an exhaustive spectral analysis of hundreds of small regional spectra over the entire SNR to establish which regions may contain metal-rich ejecta in N63A. This method is fully automated and thus significantly reduces the data analysis time, compared to a similar analysis that could have been performed with regional selections and spectral model fits "by hand". Our adaptive mesh grid can be applicable for observational data obtained at many other wavelengths. The utility of this method is not limited to SNR studies, and can be useful for the study of any extended astronomical objects (e.g., clusters of galaxies, emission nebulae, molecular clouds, etc) so long as the data have adequate photon statistics and angular resolution.

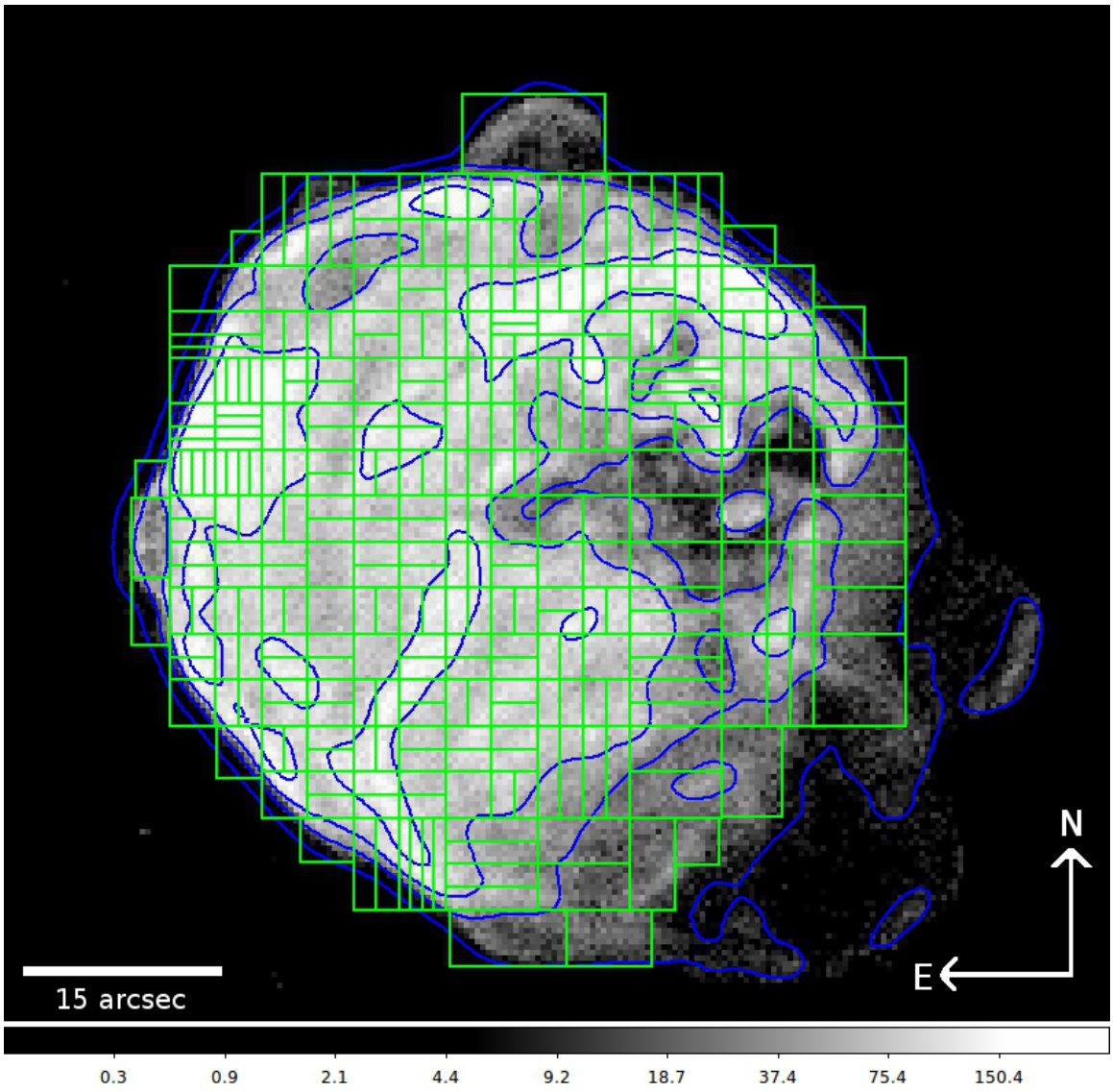

Figure 4.1 A grey-scale broadband (0.3–7.0 keV) *Chandra* ACIS image of SNR N63A. The 346 regions created by our adaptive mesh are show in green. Broadband image contours are overlaid in blue.

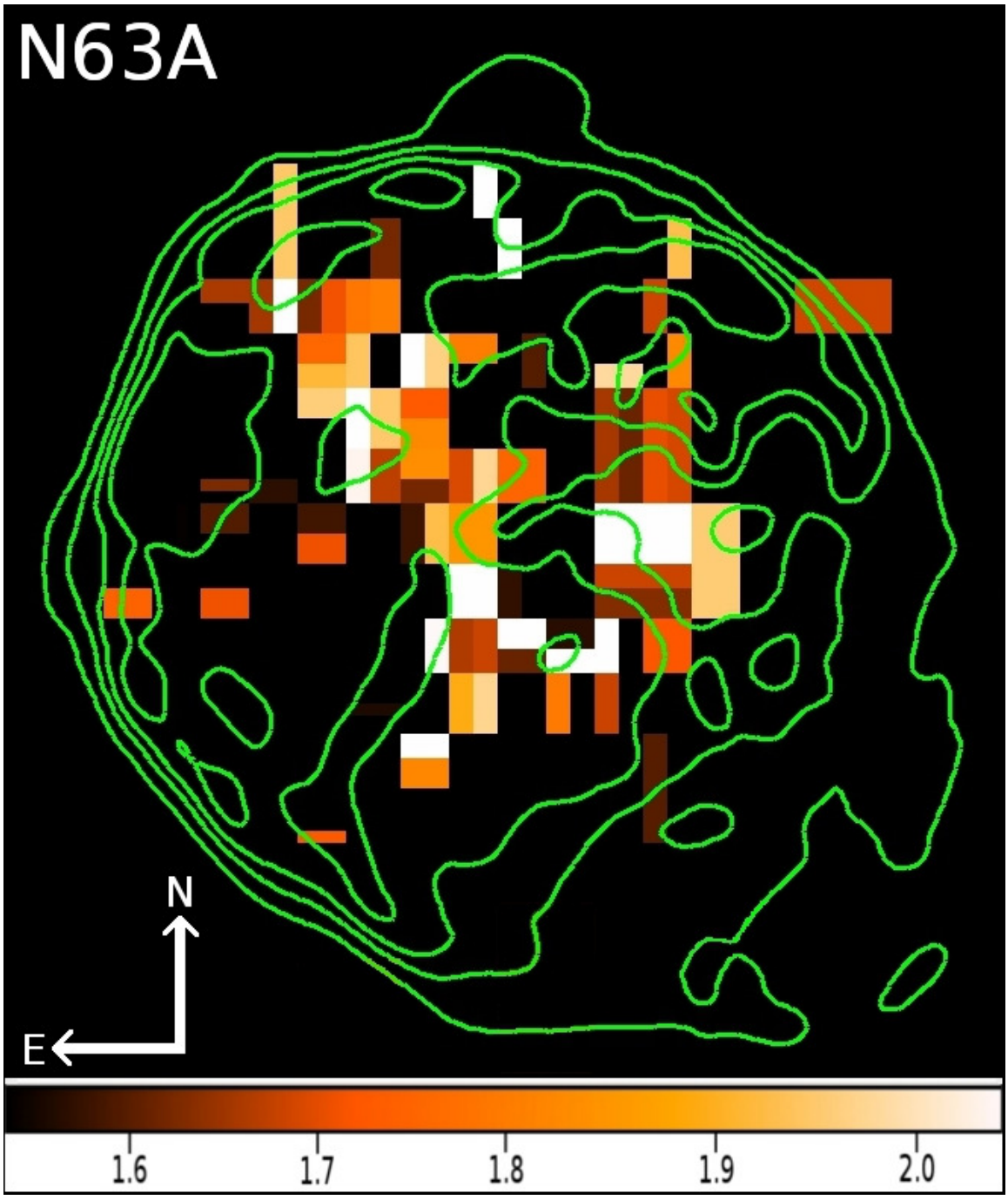

Figure 4.2 χ^2_ν map of N63A based on spectral model fits with abundances fixed at the mean LMC ISM values of this work (Table 2.2) for 346 adaptive mesh-created regions (see Section 4.2).

REFERENCES

[Aguilera et al. 2008] Aguilera, D. N., Pons, J. A., & Miralles, J. A. 2008, arXiv:0803.0486

[Anders & Grevesse 1989] Anders, E., & Grevesse, N. 1989, Geochimica et Cosmochimica Acta, 53, 197

[Aschenbach et al. 1995] Aschenbach, B., Egger, R., & Trumper, J. 1995, Nature, 373, 587

[Banes et al. 1997] Banas, K. R., Hughes, J. P., Bronfman, L., & Nyman, L. 1997, ApJ, 480, 607

[Badenes et al. 2006] Badenes, C., Borkowski, K. J., Hughes, J.P., Hwang, & U., Bravo, E. 2006, ApJ, 645, 1373

[Badenes et al. 2009] Badenes, C., Harris, J., Zaritsky, D., & Prieto, J. L. 2009, ApJ, 700, 727

[Badenes et al. 2010] Badenes, C., Maoz, D., & Draine, B. T. 2010, MNRAS, 407, 1301

[Borkowski et al. 2001] Borkowski, K. J., Lyerly, W. J., & Reynolds, S. P. 2001, ApJ, 548, 820

[Borkowski et al. 2006a] Borkowski, K. J., Hendrick, S. P., & Reynolds, S. P. 2006a, ApJ, 652, 1259

[Borkowski et al. 2007] Borkowski, K. J., Hendrick, S. P., & Reynolds, S. P. 2007, ApJ, 671, L45

[Chen et al. 2006] Chen, Y., Wang, Q. D., Gotthelf, E. V., et al. 2006, ApJ, 651, 237

[Chu & Kennicutt] Chu & Kennicutt, R. C. 1988, AJ, 96, 1874

[Chu et al. 1995] Chu, Y.-H., Dickel, J. R., Staveley-Smith, L., Osterberg, J., & Smith, R. C. 1995, AJ, 109, 1729

[Cline et al. 1982] Cline, T. L., Desai, U. D., Teegarden, B. J., et al. 1982, ApJ, 255, L45

[Cole et al. 2005] Cole, A. A., Tolstoy, E., Gallagher, III, J. S., & Smecker-Hane, T. A. 2005, AJ, 129, 1465

[Dickey & Lockman 1990] Dickey J.M., & Lockman F.J., 1990, ARA&A28, 215

[Dopita & Tuohy 1984] Dopita, M. A. & Tuohy, I. R. 1984, ApJ, 282, 135

[Filippenko 1997] Filippenko, A. V. 1997, ARA&A, 35, 309

[Foster et al. 2012] Foster, A. R., Ji, L., Smith, R. K., & Brickhouse, N. S., 2012, ApJ, 756, 128

[Gaensler et al. 2001] Gaensler, B. M., Slane, P. O., Gotthelf, E. V., & Vasisht, G. 2001, ApJ, 559, 963

[Gaensler et al. 2003] Gaensler, B. M., Hendrick, S. P., Reynolds, S. P., & Borkowski, K. J. 2003, ApJL, 594, L111

[Ghavamian et al. 2007] Ghavamian, P., Laming, J. M., & Rakowski, C. E. 2007, ApJ, 654, L69

[Gotthelf & Wang 2000] Gotthelf, E. V., & Wang, Q. D. 2000, ApJ, 532, L117

[Hendrick et al. 2003] Hendrick, S. P., Borkowski, K. J., & Reynolds, S. P. 2003, ApJ, 593, 370

[Hendrick et al. 2005] Hendrick S. P., Reynolds S. P., & Borkowski K. J., 2005, ApJ, 622, L117 (H05)

[Hillebrandt & Niemeyer 2000] Hillebrandt, W. & Niemeyer, J.C. 2000, ARA&A, 38, 191

[Hilditch et al. 2005] Hilditch, R. W., Howarth, I. D., & Harries, T. J. 2005, MNRAS,357, 304

[Hughes et al. 1995] Hughes, J. P., et al. 1995, ApJ, 444, 81

[Hughes et al. 1998] Hughes, J. P., Hayashi, I., & Koyama, K. 1998, ApJ, 505, 732 (H98)

[Hughes et al. 2003] Hughes, J. P., Ghavamian, P., Rakowski, C. E., & Slane, P. O. 2003, ApJ, 582, L95

[Hughes et al. 2006] Hughes, J. P., Rafelski, M., Warren, J. S., et al. 2006, ApJ, 645, L117

[Hwang et al. 2000] Hwang, U., Holt, S. S., & Petre, R. 2000, ApJ, 537, L119

[Hwang et al. 2001] Hwang, U., Petre, R., Holt, S. S., & Szymkowiak, A. E. 2001, ApJ, 560, 742

[Kaaret et al. 2001] Kaaret, P., et al. 2001, ApJ, 546, 1159

[Katsuda et al. 2008] Katsuda, S., Tsunemi, H., Miyata, E., Mori, K., Namiki, M., Nemes, N., & Miller, E. D. 2008b, PASJ, 60, S107

[Klose et al. 2004] Klose, S., Henden, A. A., Geppert, U., et al. 2004, ApJ, 609, L13

[Korn et al. 2000] Korn, A. J., Becker, S. R., Gummersbach, C. A., & Wolf, B. 2000, A&A, 353, 655

[Kosenko, D., Helder, E. A., & Vink, J. 2010] Kosenko, D., Helder, E. A., & Vink, J. 2010, A&A, 519, A11

[Lapenna et al. 2012] Lapenna, E., Mucciarelli, A., Origlia, L., & Ferraro, F. R. 2012, ApJ, 761, 33

[Maggie et al. 2016] Maggi, P., Haberl, F., Kavanagh, P. J., et al. 2016, A&A, 585, A162

[Manchester et al. 1993a] Manchester, R. N., Mar, D. P., Lyne, A. G., Kaspi, V. M., & Johnston, S. 1993a, ApJ, 403, L29

[Manchester et al. 1993b] Manchester, R. N., Staveley-Smith, L., & Kesteven, M. J. 1993b, ApJ, 411, 756

[Maoz et al. 2014] Maoz, D., Mannucci, F., & Nelemans, G. 2014, ARA&A, 52, 107

[McConnachie 2012] McConnachie, A. W. 2012, AJ, 144, 4

[McEntaffer et al. 2012] McEntaffer, R. L., Brantseg, T., & Presley, M. 2012, ApJ, 756, 17

[McKee 1974] McKee, C. F. 1974, ApJ, 188, 335

[Mereghetti 2011] Mereghetti, S. 2011, in High-Energy Emission from Pulsars and their Systems, ed. D. F. Torres & N. Rea, 345

[Middleditch & Pennypacker 1985] Middleditch, J., & Pennypacker, C. R. 1985, Nature, 313, 659

[Miyata et al. 2001] Miyata, E., Tsunemi, H., Aschenbach, B., & Mori, K. 2001, ApJ, 559, L45

[Morse, Winkler, & Kirshner 1995] Morse, J. A., Winkler, P. F., & Kirshner, R. P., 1995 AJ 109, 2104

[Nomoto et al. 2006] Nomoto, K., Tominaga, N., Umeda, H., Kobayashi, C., & Maeda, K. 2006, Nuclear Physics A, 777, 424

[Park et al. 2002] Park, S., Roming, P. W. A., Hughes, J. P., et al. 2002, ApJ, 564, L39

[Park et al. 2003a] Park, S., Burrows, D. N., Garmire, G. P., et al. 2003a, ApJ, 586, 210

[Park et al. 2003b] Park, S., Hughes, J. P., Slane, P. O., et al. 2003b, ApJ, 592, L41

[Park et al. 2003c] Park, S., Hughes, J. P., Burrows, D. N., Slane, P. O., Nousek, J. A., & Garmire, G. P. 2003, ApJ, 598, L95

[Park et al. 2007] Park, S., Hughes, J. P., Slane, P. O., et al. 2007, ApJ, 670, L121

[Park et al. 2010] Park, S., Hughes, J. P., Slane, P. O., et al. 2010, ApJ, 710, 948

[Park et al. 2012] Park, S., Hughes, J. P., Slane, P. O., et al. 2012, ApJ, 748, 117

[Petre et al. 2007] Petre, R., Hwang, U., Holt, S. S., Sa-Harb, S., & Williams, R. M. 2007, ApJ, 662, 988

[Pietrzynski et al. 2013] Pietrzynski, G., Graczyk, D., Gieren, W., et al. 2013, Nature, 495, 76

[Pompia et al. 2009] Pompia, L., Hill, V., Spite, M., et al. 2008, A&A, 480, 379

[Reynolds 2008] Reynolds, S. R. 2008, ARA&A, 46, 89

[Reynolds & Chevalier, 1981] Reynolds, S. P., & Chevalier, R. A. 1981, ApJ, 245, 912

[Reynolds & Chevalier, 1984] Reynolds, S. P., & Chevalier, R. A. 1984, ApJ, 278, 630

[Rothschild et al. 1994] Rothschild, R. E., Kulkarni, S. R., & Lingenfelter, R. E. 1994, Nature, 368, 432

[Russell & Dopita 1992] Russell, S. C., & Dopita, M. A. 1992, ApJ, 384, 508 (RD92)

[Schenck et al. 2014] Schenck, A., Park, S., Burrows, D., et al. 2014, ApJ, 791,50

[Schenck et al. 2016] Schenck, A., Park, S., & Post, S. 2016, AJ, 151, 161

[Sedov 1959] Sedov, L. I., 1959, Similarity and Dimensional Methods in Mechanics (New York: Academic)

[Smith et al. 2001] Smith, R. K., Brickhouse, N.found S., Liedahl, D. A., & Raymond, J. C. 2001, ApJ, 556, L91

[Sonneborn et al. 1987] Sonneborn, G., Altner, B., & Kirshner, R. P. 1987, ApJ, 323, L35

[Warren et al. 2003] Warren, J. S., Hughes, J. P., & Slane, P. O. 2003, ApJ, 583, 260

[Weisskopf et al. 2003] Weisskopf, M. C., Aldcroft, T. L., Bautz, M., et al. 2003, Experimental Astronomy, 16, 1

[Weisskopf & Hughes 2006] Weisskopf, M. C., & Hughes, J. P. 2006, in Astrophysics Update 2, ed. J. W. Mason (Heidelberg: Springer), 55

[Williams & Chu 2005] Williams, R. M., & Chu, Y.-H. 2005, ApJ, 635, 1077

[Williams et al. 2005] Williams, R. M., Chu, Y.-.H., Dickel, J. R., et al. 2005, ApJ, 628, 704

[Vancura et al. 1992] Vancura, O., Blare, W. P., Long, K. S., & Raymond, J. C. 1992, ApJ, 394, 158

[Yakovlev et al. 2004] Yakovlev, D. G., & Pethick, C. J. 2004, ARA&A, 42, 169